Applied Catalysis B: Environmental 221 (2018) 56–69

Contents lists available at ScienceDirect

Applied Catalysis B: Environmental

journal homepage: www.elsevier.com/locate/apcatb

Research paper

# Novel hybrids of graphitic carbon nitride sensitized with *free-base meso*-tetrakis(carboxyphenyl) porphyrins for efficient visible light photocatalytic hydrogen production

Eliana S. Da Silva[a,*], Nuno M.M. Moura[b], M. Graça P.M.S. Neves[b], Ana Coutinho[c,d], Manuel Prieto[c], Cláudia G. Silva[a], Joaquim L. Faria[a,*]

[a] *Laboratory of Separation and Reaction Engineering – Laboratory of Catalysis and Materials (LSRE-LCM), Faculdade de Engenharia, Universidade do Porto, Rua Dr. Roberto Frias s/n 4200-465 Porto, Portugal*

[b] *QOPNA, Department of Chemistry, University of Aveiro, 3810-193 Aveiro, Portugal*

[c] *Centro de Química-Física Molecular and Institute of Nanoscience and Nanotechnology, Instituto Superior Técnico, Universidade de Lisboa, Av. Rovisco Pais, 1049-001 Lisboa, Portugal*

[d] *Dep Química e Bioquímica, Faculdade de Ciências, Universidade de Lisboa, Campo Grande, 1749-016 Lisboa, Portugal*

ARTICLE INFO

*Keywords:*
*Free-base* porphyrins
Graphitic carbon nitride
Hydrogen production
Photocatalysis
Water splitting

ABSTRACT

Novel hybrid photocatalysts of graphitic carbon nitride (g-$C_3N_4$, CN) sensitized with *free-base* porphyrins were prepared by impregnation through non-covalent interactions. Their photocatalytic activity was evaluated towards the generation of hydrogen ($H_2$) from water splitting. For this purpose, and in order to ascertain the influence of the carboxy substituents groups and their position on the porphyrin periphery on $H_2$ production, the porphyrins *meso*-tetraphenylporphyrin (TPP), *meso*-tetrakis(*meta*-carboxyphenyl)porphyrin (*m*TCPP) and *meso*-tetrakis(*para*-carboxyphenyl)porphyrin (*p*TCPP) were used. All the hybrids (TPP-CN, *m*TCPP-CN and *p*TCPP-CN) show higher performance for photocatalytic $H_2$ production than that of pure CN. Among all the hybrids, *m*TCPP-CN presents the highest amount of $H_2$ evolved, being of 326 and 48.4 μmol under 6 h of UV–vis and visible light ($\lambda > 400$ nm) irradiation, respectively. This photocatalyst was fully characterized by UV-vis, FTIR, XRD, XPS, SEM, TEM, $N_2$ isotherms and steady-state and time-resolved fluorescence measurements. The fluorescence emission of the *m*TCPP porphyrin was remarkably quenched by CN semiconductor for the various hybrids *m*TCPP-CN containing different amounts of *m*TCPP, consistent with electron injection from the porphyrin excited state into the conduction band of the semiconductor. This works demonstrates that the sensitization of CN with dye porphyrins enhances the photocatalytic $H_2$ evolution under UV–vis and visible light irradiation, making it a potential material for solar conversion to produce hydrogen from water.

## 1. Introduction

The demand for energy is increasing with growing global population which is projecting toward 10.6 billion by 2050 [1]. In order to meet this challenge, and due to the gradual depletion of fossil fuel reserves and emission of greenhouse gases, the conventional hydrogen ($H_2$) production *via* steam reforming of fossil fuels has to be replaced by sustainable and environmentally friendly technologies. Among various potential solutions, solar $H_2$ production from water splitting using photocatalysts inspired in the natural process of photosynthesis [2–4] holds great promise as an environmentally clean energy for the future since it can be simultaneous considered as a method for both solar energy storage and chemical energy conversion [5,6]. In the last years many catalysts have been designed and applied for hydrogen production. Yet, and despite all the advances that are being achieved, the quest for photocatalysts able to promote a high and efficient conversion of solar energy into chemical energy is still a challenge.

Over this infinity of compounds [7,8], the metal-free polymeric semiconductor graphitic carbon nitride, g-$C_3N_4$ [9], is regarded as the shining star due to its appealing features, which enable it to be employed both in energy conversion [9–11] and environmental remediation [12]. Among other features, g-$C_3N_4$ possesses valence (VB) and conduction (CB) band potentials suitable for both water reduction and oxidation (+1.4 V and −1.3 V *vs.* NHE at pH 7, respectively) [13,14], presents good chemical and physical stability and it is easy to synthesize from low-cost and environmentally friendly precursors, such as

* Corresponding authors.
*E-mail addresses:* eliana@fe.up.pt (E.S. Da Silva), jlfaria@fe.up.pt (J.L. Faria).

http://dx.doi.org/10.1016/j.apcatb.2017.08.079
Received 21 June 2017; Received in revised form 15 August 2017; Accepted 23 August 2017
Available online 14 September 2017
0926-3373/ 

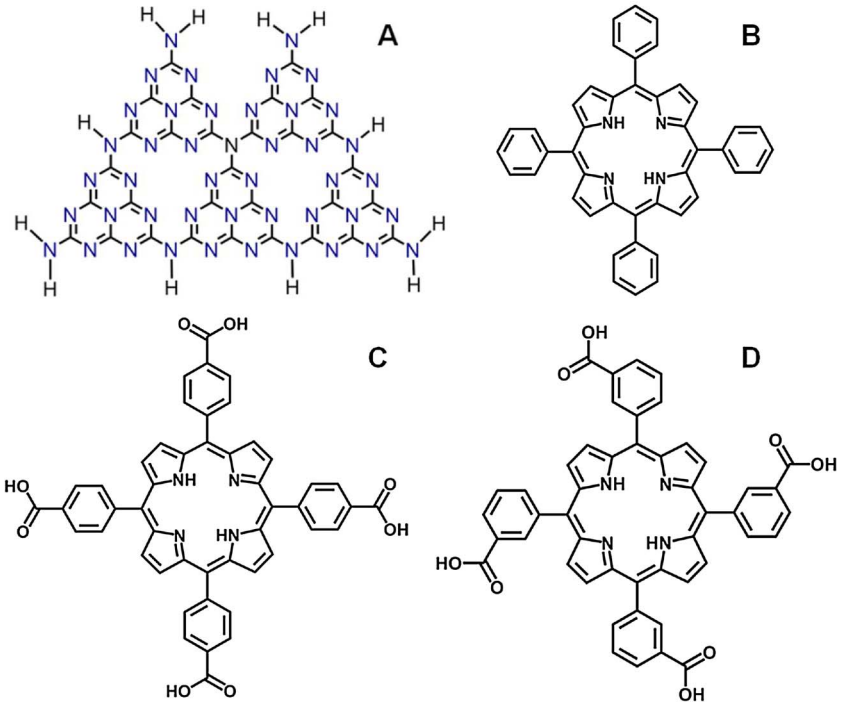


**Fig. 1.** Chemical structures of the semiconductor CN (A) and of the porphyrins TPP (B), *p*TCPP (C) and *m*TCPP (D).

urea, dicyandiamide, cyanamide, thiourea and melamine [12,15]. Although it presents some absorption in the visible region, its band gap (~ 2.7 eV) largely restricts its solar light application. Moreover, the high degree of recombination between photoinduced electrons ($e^-$) and holes ($h^+$) also hampers its practical application. Therefore, it is mandatory to find alternatives for overcoming these disadvantages. Some of the methods proposed to increase the photocatalytic activity of g-$C_3N_4$ include heteroatom doping [16], metal loading [17], coupling with carbon materials such as carbon nanotubes [18] and graphene derivatives [19] and sensitization with organic dyes [20]. Among these strategies, dye sensitization is considered an efficient route, not only to extend the spectral response region of wide band gap semiconductors, enabling more efficient visible light harvesting, but also to enhance the separation and transport of photogenerated electrons and holes at the semiconductor dye interface [21,22], a key factor to obtain better photocatalytic activity. The efficiency of these systems depends on both the properties of the sensitizers and semiconductor, and their interaction upon photoexcitation [20]. Porphyrins and phthalocyanines [23] have merited much attention as dye sensitizers owing to their physical-chemical properties, enabling their use in diverse fields such as in dye sensitized solar cells (DSSCs) [23], medicine (*e.g.* photodynamic therapy of cancer [24,25] and photoinactivation of microorganisms [26]), photoelectronic devices [27], sensors [28–30], environmental remediation [31], $CO_2$ reduction [32] and photocatalytic $H_2$ generation [33,34]. These coloured organic macrocycles exhibit high absorption coefficient in the visible and near IR region (where the maximum of the solar photon flux occurs), that is necessary for efficient photon harvesting, rich redox properties, good chemical stability when compared with other dyes and photoinduced electron transfer and semiconducting capabilities [35]. Indeed, the metalloporphyrin derivative chlorophyll is the paradigm for solar to chemical energy conversion [36]. The ability to tune the photophysical properties of synthetic porphyrins, by modifying the electronic distribution on the aromatic ring via peripheral substitution, led to the design and understanding of numerous porphyrin photonic assemblies which mimic photosynthetic solar energy transduction by converting solar energy into chemical potential in the form of long-lived charge separation states [37]. The sensitization of g-$C_3N_4$ has been reported using dyes such Erythrosin [38], Eosin Y [39], phthalocyanines [39–41] and porphyrins [42,43]. For instance, Chen *et al.* [42] reported a simple method to assemble Cu (II)*meso*-tetra(4-carboxyphenyl)porphyrin (CuTCPP) on the surface of g-$C_3N_4$ through a non covalent approach, which promotes visible-light harvesting and enhances the visible light photocatalytic activity towards phenol degradation. Another study carried out by Wang and coworkers [43] reported the synthesis of a pure organic heterostructure of g-$C_3N_4$/$(FeTPP)_2O$, in which the porphyrin $(FeTPP)_2O$ acted not just as a photosensitizer but also played the role of charge promoter, inhibiting the $e^-/h^+$ pair recombination, and leading to an outstanding photocatalytic $H_2$ production efficiency under solar light irradiation without using any co-catalysts (52.9 μmol $H_2$, 4 h). Zhang *et al.* [41] reported the sensitization of g-$C_3N_4$ by combining an asymmetric zinc phthalocyanine derivative with an organic dye for the photocatalytic $H_2$ production in the visible/near-infrared region. That work puts in evidence the added value of combining two photosensitizers over one semiconductor for the photocatalytic generation of $H_2$. Zhu *et al.* [44] reported the non-covalent immobilization via $\pi$-$\pi^*$ stacking interactions of porphyrin over reduced graphene oxide (RGO) nanosheets to obtain the porphyrin/RGO nanocomposite. Porphyrin moiety in the nanocomposite acts as a photosensitizer harvesting light. This composite shows remarkable photocatalytic activity under UV–vis light irradiation attributed to the fast electron transfer from the photoexcited porphyrin molecules to RGO sheets.

Herein, we report the preparation and characterization of g-$C_3N_4$ (henceforth abbreviated as CN) sensitized with *free-base* porphyrins for the efficient photocatalytic $H_2$ generation through water splitting. Although these materials present interesting characteristics for photocatalytic applications, porphyrin-sensitized CN has not yet received wide attention, which boosted our interest in exploring this theme. In fact, and to the best of our knowledge, this is the first study using *free-base* porphyrins as CN dye sensitizers for photocatalytic $H_2$ production. Three different porphyrins were used in the present work (Fig. 1): *meso*-tetraphenylporphyrin (TPP), *meso*-tetrakis(*meta*-carboxyphenyl)porphyrin (*m*TCPP) and *meso*-tetrakis(*para*-carboxyphenyl)porphyrin (*p*TCPP).

The porphyrins were immobilized over CN by a simple impregnation method in order to obtain hybrid photocatalysts of TPP-CN, *m*TCPP-CN and *p*TCPP-CN. Furthermore, the electron transfer process from the excited state porphyrin to the CB of CN was investigated by

absorption, steady-state and time-resolved fluorescence measurements. All the hybrids are able to promote the production of $H_2$ under UV–vis and visible light irradiation, and the rate of production is dependent on the type and amount of porphyrin loaded on CN. The best performing hybrid photocatalyst (*m*TCPP-CN) was selected to further elucidate the mechanism of $H_2$ production.

## 2. Experimental section

### 2.1. Materials and chemicals

Dicyandiamide (99%), L-ascorbic acid (99%), barium sulfate (98%), ethylenediaminetetraacetic acid (EDTA, ≥ 98%), hydrochloric acid (≥ 37%), pyrrole (98%), benzaldehyde (98%), methyl 3-formylbenzoate (98%) and 4-formylbenzoic acid (97%) were purchased from Sigma-Aldrich and used without further purification. Dihydrogen hexachloroplatinate (IV) hexahydrate was purchased from Alfa Aesar, sodium hydroxide from José Manuel Gomes dos Santos, and ethanol, methanol and *N,Ń*-dimethylformamide (DMF) from Fischer Chemical. Ultrapure water obtained from a Millipore Milli-Q system water purification system (≥ 18 MΩ $cm^{-1}$) was implemented throughout all assays. EDTA aqueous solution was prepared in NaOH (0.5 mol $L^{-1}$). Solvents used in the synthesis of porphyrins were purchased from Panreac and Riedel-de-Häen and used as received or distilled and dried by using standard procedures according to the literature [45].

### 2.2. Catalyst preparation

#### 2.2.1. Synthesis of meso-tetraphenylporphyrin (TPP)

TPP was prepared in 28% yield by condensation of pyrrole and benzaldehyde following a well-established protocol [46–48]. The structure of TPP was confirmed by $^1$H NMR, mass spectrometry and UV–vis techniques. The experimental data are in agreement with the one described in literature. $^1$H NMR (300 MHz, $CDCl_3$): $\delta$ 8.85 (8H, s, H-β), 8.23-8.20 (8H, m, H-*o*-Ph), 7.78-7.66 (12H, m, H-*m*,*p*-Ph), −2.77 (2H, s, *N*-H) ppm. MS [ESI(+)]: *m/z* 614.2 $[M]^{+\cdot}$. UV–vis (DMF): $\lambda_{max}$ (log ε) 416 (5.27), 512 (4.09), 546 (3.75), 590 (3.57), 647 (3.55) nm.

#### 2.2.2. Synthesis of meso-tetrakis(m-carboxyphenyl)porphyrin (mTCPP)

*m*TCPP was obtained by basic hydrolysis of the corresponding methyl ester derivative [49]. This precursor was prepared by refluxing pyrrole (4 mL, $3.9\times10^{-3}$ mol) with methyl 3-formylbenzoate (0.640 g, $3.9\times10^{-3}$ mol) in a mixture of acetic acid (120 mL) and nitrobenzene (70 mL) for 1 h. After this period, the reaction mixture was cooled to room temperature and then it was added methanol. The resulting solid was collected by vacuum filtration and after being dried afforded the desired m*eso*-tetrakis(*m*-carbomethoxy)phenylporphyrin in 27% yield. $^1$H NMR (300 MHz, $CDCl_3$): $\delta$ 8.90 (4H, t, $J$ = 1.5 Hz, H-2′), 8.80 (8H, s, H-β), 8.49 (4H, dt, $J$ = 1.5 and 7.8 Hz, H-4′), 8.41 (4H, dt, $J$ = 1.5 and 7.8 Hz, H-6′), 7.86 (4H, t, $J$ = 7.8 Hz, H-5′), 3.99 (12H, s, $CO_2CH_3$), −2.80 (2H, s, *N*-H) ppm. MS [ESI(+)]: *m/z* 844.3 $[M]^{+\cdot}$. UV–vis (DMF): $\lambda_{max}$ (log ε) 417 (5.52), 512 (3.34), 546 (3.30), 589 (3.28), 645 (3.23) nm.

The hydrolysis of the ester groups was performed by adding KOH (400 equiv.) dissolved in a mixture of MeOH (10 mL) and pyridine (0.75 mL) to a solution of *meso*-tetrakis(*m*-carbomethoxy)phenylporphyrin (300 mg, $3.5\times10^{-4}$ mol) in THF (25 mL). Then, the mixture was maintained under stirring for 1 h at 80 °C. After cooling to room temperature, the reaction mixture was partitioned between an aqueous solution of citric acid and $CH_2Cl_2$. The organic layer was separated, washed with water, dried with $Na_2SO_4$ and the solvent evaporated under reduced pressure. After crystallization from $CH_2Cl_2$/hexane the desired *meso*-tetrakis(*m*-carboxyphenyl)porphyrin (*m*TCPP) was isolated in 95%. $^1$H NMR (300 MHz, DMSO-$d_6$): $\delta$ 8.91 (8H, s, H-β), 8.78 (4H, s, H-2′), 8.61-8.54 (4H, m, H-4′), 8.49 (4H, dt, $J$ = 1.4 and 7.8 Hz, H-6′), 8.04 (4H, t, $J$ = 7.8 Hz, H-5′), −2.86 (2H, s, *N*-H) ppm. MS [ESI(+)]: *m/z* 844.3 $[M]^{+\cdot}$. UV–vis (DMF): $\lambda_{max}$ (log ε) 419 (5.61), 514 (4.23), 548 (3.89), 589 (3.77), 645 (3.56) nm.

#### 2.2.3. Synthesis of meso-tetrakis(p-carboxyphenyl)porphyrin (pTCPP)

*p*TCPP was prepared in 57% from the condensation in acidic medium of pyrrole with 4-formylbenzoic acid according with a methodology previously described [50]. The structure of *p*TCPP was confirmed by $^1$H NMR mass spectrometry and UV–vis techniques and the spectroscopic data is in agreement with literature data [50]. $^1$H NMR (300 MHz, DMSO-$d_6$): $\delta$ 13.3 (4H, s, $-CO_2H$), 8.87 (8H, s, H-β), 8.40 and 8.35 (16H, AB system, $J$ = 8.3 Hz, Ar-*o*,*m*-H), −2.94 (2H, s, *N*-H) ppm. MS [ESI(+)]: *m/z* 844.3 $[M]^{+\cdot}$. UV–vis (DMF): $\lambda_{max}$ (log ε) 418 (5.69), 513 (4.25), 547 (3.96), 587 (3.80), 644 (3.69) nm.

#### 2.2.4. Synthesis of graphitic carbon nitride (CN)

Bulk CN was synthesized by a solid state-thermal method using dicyandiamide as precursor. In a typical synthesis, the precursor was placed in a semi-closed crucible inside a muffle furnace and heated under static air at 450 °C for 2 h with a ramping rate of 2 °C $min^{-1}$, then heating up to 550 °C and maintaining this temperature for 4 h. The *as*-prepared light yellow CN powder was washed with water to remove any unreacted precursor, dried overnight at 100 °C and ground into powder to further use.

#### 2.2.5. Preparation of porphyrin-CN hybrid catalysts

The porphyrin-CN hybrids were synthesized by an impregnation method. In a typical procedure, a certain amount of CN was dispersed in ethanol and stirred for 30 min. A given amount of porphyrin was then added to this suspension and the mixture was stirred vigorously for 8 h at room temperature. After volatilization of the ethanol, the powder was washed and dried in an oven at 60 °C overnight. Hybrids of TPP-CN, *m*TCPP-CN and *p*TCPP-CN containing a 16.7% weight ratio (wt.%) of the respective porphyrin were prepared following the above described procedure. Other *m*TCPP-CN hybrids were prepared with lower *m*TCPP porphyrin content, namely 9.1, 6.3 and 4.8 wt.%. The *as*-prepared hybrid composites are labeled hereafter as Xporphyrin-CN, being X the wt.% of porphyrin present in the hybrid followed by the acronyms of the porphyrins. Nonetheless, for sake of clarity, the 16.7, 9.1, 6.3 and 4.8 wt.% of porphyrin present in the hybrid are from now on designated as 17, 9, 6 and 5%, respectively. As so, the hybrids are labeled as 17TPP-CN, 17*m*TCPP-CN, 17*p*TCPP-CN, 9*m*TCPP-CN, 6*m*TCPP-CN and 5*m*TCPP-CN.

#### 2.2.6. Synthesis of platinum nanoparticles

The synthesis of colloidal platinum (Pt) particles was performed according to a previous reported procedure [51]. In a typical synthesis, an aqueous solution of dihydrogen hexachloroplatinate (IV) hexahydrate (60 mg in 20 mL of water) was added dropwise to a methanol solution containing L-ascorbic acid (600 mg in 180 mL of methanol). The mixture was heated with constant stirring under reflux during 3 h. After cooling, the suspension was centrifuged and the solid washed twice with fresh methanol. Afterward, the solid was dried at room temperature and was finally resuspended in a certain volume of water.

### 2.3. Catalysts characterization

$^1$H NMR solution spectra were recorded on a Bruker Avance 300 (300.13 MHz) spectrometer. $CDCl_3$ or DMSO-$d_6$ was used as the solvent and tetramethylsilane (TMS) as an internal reference. Chemical shifts are expressed in δ (ppm) and the coupling constants ($J$) in Hertz (Hz). Electrospray ionization mass spectra were acquired with a Micromass Q-Tof 2 (Micromass, Manchester, UK), operating in the positive ion mode, equipped with a Z-spray source, an electrospray probe and a syringe pump. Source and desolvation temperatures were 80 °C and 150 °C, respectively. Capillary voltage was 3000 V. The spectra were acquired at a nominal resolution of 9000 and at cone voltages of 30 V.

Nebulisation and collision gases were $N_2$ and Ar, respectively. Porphyrin solutions in methanol were introduced at a 10 μL $min^{-1}$ flow rate. UV–vis absorption spectra of solutions were recorded on a UV–vis spectrophotometer (Jasco V-560) using a 1 cm path length quartz Suprasil cuvette. Solid samples were analyzed by UV–vis diffuse reflectance spectroscopy (UV-vis DRS) using the same spectrophotometer equipped with an integrating sphere attachment (JASCO ISV-469). $BaSO_4$ was used as the reflectance standard reference and the absorption spectra were calculated from the reflectance data with the Kubelka-Munk function. The molecular structural information of the catalytic materials was collected using a JASCO Fourier Transform Infrared spectroscopy (FT/IR-6800) in attenuated total reflectance (ATR) mode. Each spectrum was collected at room temperature, after 256 scans taken at 4 $cm^{-1}$ resolution in the range 600–4000 $cm^{-1}$, and analyzed using JASCO Spectra Manager™ II cross-platform software. X-ray diffraction (XRD) analysis was carried out in a PANalytical X'Pert MPD equipped with a X'Celerator detector and secondary monochromator (CuKα = 0.154 nm, 40 kV, 30 mA; data recorded at a 0.017° step size, 100 s/step). The Brunauer-Emmett-Teller (BET) specific surface area ($S_{BET}$) was measured from $N_2$ adsorption-desorption isotherms at 77 K in a Quantachrome Nova 4200e apparatus. Prior to measurements, the samples were out-gassed at 120 °C for 5 h. The pore size distributions of the materials were obtained by using the Barrett-Joyner-Halenda (BJH) method using adsorption branch. Elemental analysis was performed using an Elementar Vario MICRO and OXY cube equipment. X-ray photoelectron spectroscopy (XPS) analysis were carried out in a Kratos AXIS Ultra HSA equipment using an Al monochromator as the X-ray source operating at 15 kV (90 W) in hybrid mode. All of the binding energies were calibrated by C1s peak at 285.0 eV. The morphology of the samples was analyzed on a Jeol JEM-2200FS transmission electron microscope (TEM) operated at 200 kV and Hitachi SU-70 scanning electron microscopy in the transmission mode (STEM) operated at 30 kV. Steady-state photoluminescence (PL) spectra of pure *m*TCPP, CN and of *m*TCPP-CN hybrid photocatalysts, as well as the fluorescence quenching measurements, were recorded at room temperature on a JASCO FP-8300 spectrofluorometer equipped with a 150 W Xe lamp. Samples were excited at different wavelengths of absorption using bandwidth slits of 10 nm. The fluorescence intensity decays of pure *m*TCPP, CN and the hybrids were measured in water using the time-correlated single-photon timing technique. The samples were excited at 340 nm using a frequency-doubled laser of Rhodamine 6G (Coherent 701-2). The fluorescence decays were measured with an emission polarizer set at the magic angle at 450 or 650 nm using a Jobin-Yvon HR320 monochromator and a Hamamatsu R-2809U microchannel plate. The instrument response function (IRF) was recorded as excitation light scattered by a Ludox dispersion (silica, colloidal water solution, Aldrich, Milwaukee, WI). The data was acquired in a multichannel analyzer with a time window of 1024 channels using a time-scale of 24.4 or 48.8 ps/channel, respectively. Typically 50.000 and 20.000 counts were acquired in the peak channels of the IRF and sample decay curves, respectively. The fluorescence decay parameters (normalized amplitudes, α, and lifetimes, $\tau$) were determined using the TRFA Data Processing Package (version 1.4) of the Scientific Software Technologies Center (Belarusian State University, Belarus) by fitting the fluorescence intensity decays, $I(t)$, to a sum of $n$ exponentials (Eq. (1)):

$$I(t) = \sum_{i=1}^{n} \alpha_i exp(-t/\tau_i) \quad (1)$$

The fits tabulated represent the minimum set of adjustable parameters that satisfy the usual statistical criteria, namely a reduced $\chi^2$ value < 1.3 and a random distribution of weighted residuals. The intensity-weighted average lifetime, $\tau_{av}$, was calculated according to Eq. (2):

$$\tau_{av} = \sum_{i=1}^{n} \alpha_i \cdot \tau_i^2 / \sum_{i=1}^{n} \alpha_i \cdot \tau_i \quad (2)$$

### 2.4. Photocatalytic tests

The photocatalytic experiments for $H_2$ production were carried out at room temperature in a cylindrical glass immersion photo-reactor equipped with a Heraeus TQ 150 medium pressure mercury vapour lamp located axially in the reactor and held in a quartz immersion tube. A DURAN 50® glass cooling jacket was used for irradiation in the near UV to visible light range (emission lines at 365, 405, 435, 546 and 578 nm). A liquid UV cut-off filter ($NaNO_2$ 1.0 mol $L^{-1}$) was used to produce visible light (emission lines at 405, 435, 546 and 578 nm). The irradiance of the lamp was measured using a calibrated Modular USB series spectrometer from Ocean Optics, either in absence (UV-vis light, 550 W $m^{-2}$) or presence of the cut-off filter (visible light, 370 W $m^{-2}$). A typical photoreaction was performed using 150 mL of an aqueous suspension containing 15 mg of catalyst, EDTA ($2.0 \times 10^{-2}$ mol $L^{-1}$) as sacrificial electron donor and Pt ($6.1 \times 10^{-5}$ mol $L^{-1}$) as co-catalyst, at natural pH conditions (pH ~ 6.1). Before irradiation, the catalyst suspension was dispersed in an ultrasonic bath for 5 min. The suspension was continuously stirred and de-aerated by blowing with nitrogen during 40 min prior to irradiation to ensure total removal of dissolved oxygen. These conditions were maintained throughout the irradiation time. The solution was maintained at room temperature (~ 25 °C) by a cooling water flow during the course of reaction. The amount of $H_2$ evolved was measured using an on-line gas chromatograph (Inficon Micro GC 3000) equipped with a molsieve column and a micro-TCD detector, using argon as carrier gas. Measurements were taken each five minutes during a six hour period. When needed, the pH of the solutions was adjusted prior to irradiation either by adding hydrochloric acid (0.5 mol $L^{-1}$) or sodium hydroxide (0.5 mol $L^{-1}$). For reuse experiments, the irradiated solution was centrifuged and the remaining catalyst was washed with water. Afterwards, new fresh solution containing EDTA and Pt was added to the catalyst and oxygen was removed by bulling nitrogen prior to start a new irradiation cycle. This procedure was repeated for four consecutive cycles.

## 3. Results and discussion

Hybrids of CN sensitized with porphyrins containing *meso*-phenyl groups (TPP) and *meso*-phenyl groups bearing *meta*- and *para*-carboxy substituents (*m*TCPP and *p*TCPP, respectively) have been synthesized and investigated for the first time for photocatalytic $H_2$ production. The carboxyphenyl group is one of the most commonly used functional group in dye sensitized semiconductors since it facilitates the electron injection to the CB of the semiconductor [52]. In this context, many light-harvesting supramolecular assemblies have been built up by non-covalent interaction of dyes and carbon based materials, and applied with success for the photochemical $H_2$ production [53,54]. This strategy of synthesis was adopted in this work rather than covalent interactions since it combines the unique features of each molecule and preserves the intrinsic properties of both moieties, in addition to being a straightforward and easy preparation method [54]. The synthesis of porphyrin-CN hybrid photocatalysts was therefore performed by impregnation in which the porphyrin was assembled over CN surface via non-covalent interactions, such as electrostatic interactions and π-π* stacking interactions [42]. However, and due to the 18-π-electron aromatic structure of porphyrins, their immobilization over CN is most probably driven by π-π* stacking interactions. The characterization of these hybrid materials and their photocatalytic activity for $H_2$ production from water are given in next sections.

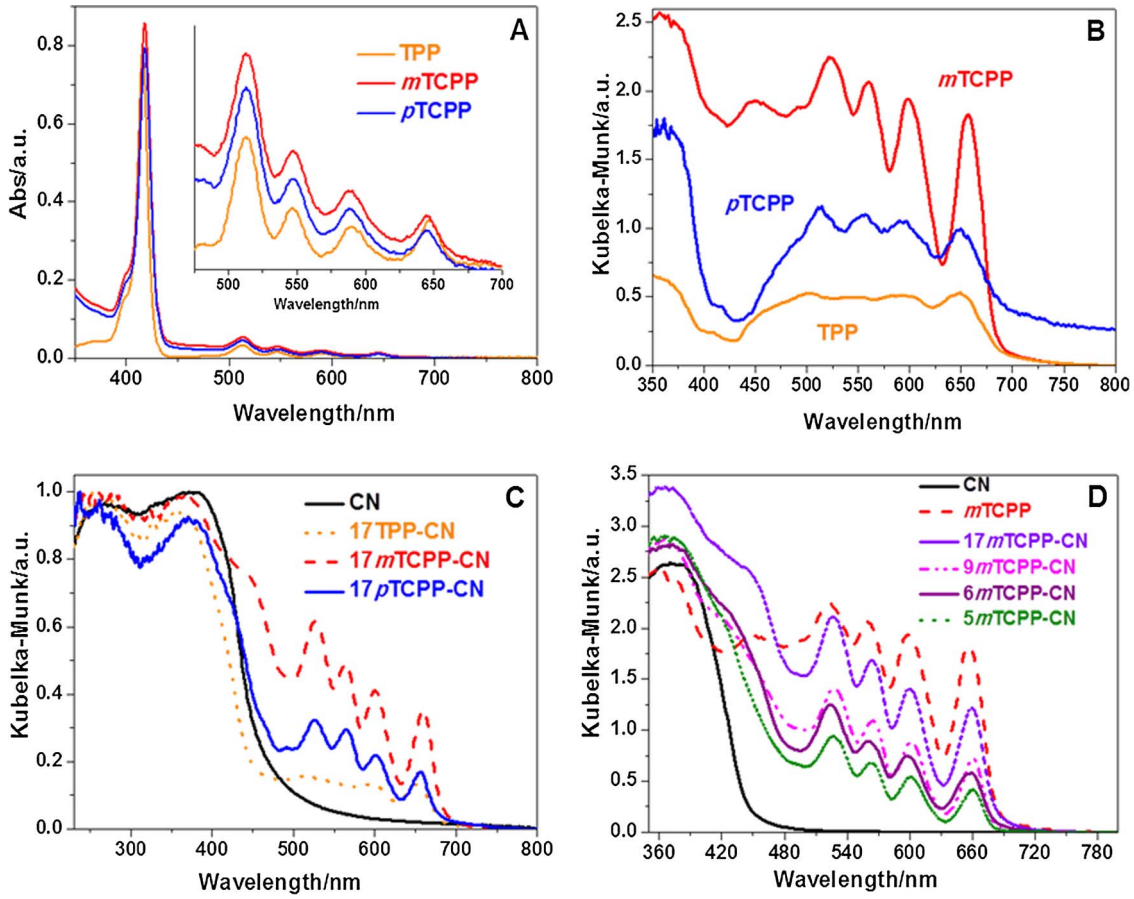


**Fig. 2.** (A) UV–vis absorption spectra of the porphyrins TPP, *m*TCPP and *p*TCPP in DMF solution ($2.0 \times 10^{-6}$ mol $L^{-1}$). The inset is an expanded view of the spectral region of Q-bands. UV–vis DRS of: (B) the porphyrins TPP, *m*TCPP and *p*TCPP, (C) pure CN and 17TPP-CN, 17*m*TCPP-CN, 17*p*TCPP-CN hybrids, (D) pure CN and *m*TCPP, and of *m*TCPP-CN hybrids with different contents of *m*TCPP.

### 3.1. Characterization of the catalytic materials

Several techniques, such as UV–vis absorption, Fourier transform infrared (FTIR), X-ray diffraction (XRD), X-ray photoelectron spectroscopy (XPS), Scanning and Transmission electron microscopy (SEM and TEM) and photoluminescence (PL), were employed to study the morphology, and the optical and photophysical properties of the pure semiconductor CN and pure porphyrins TPP, *m*TCPP and *p*TCPP, as well as of the *as*-prepared hybrids. Fig. 2A presents the UV–vis absorption spectra of the *free-base* porphyrins TPP, *m*TCPP and *p*TCPP in DMF solution while Table 1 summarizes its peak positions. All the porphyrins present strong absorption in the visible region, ranging from 400 to 700 nm, typical for this type of compounds [35]. The peak centered at around 420 nm is attributed to the Soret absorption band arising from the $a_{1u}(\pi)$-$e_g(\pi)$ transition ($S_0$-$S_2$), while the four absorption bands between 500 and 700 nm are ascribed to the weaker Q bands of $a_{2u}(\pi)$-$e_g(\pi)$ transitions ($S_0$-$S_1$) [55]. These B and the Q bands arising from π–π* transitions and can be rationalized by considering the Gouterman four orbital model (HOMO and LUMO orbitals) [35] and are in accordance with literature data [56].

**Table 1**
UV–vis absorption spectral data of *free-base* porphyrins TPP, *m*TCPP and *p*TCPP and of the various *m*TCPP-CN hybrids in DMF (l) and in solid state (s).

| Compound | Soret band (nm) | Q bands (nm) | | | |
|---|---|---|---|---|---|
| | | I | II | III | IV |
| TPP | 416 (l) | 512 (l) | 546 (l) | 590 (l) | 647 (l) |
| *p*TCPP | 418 (l) | 513 (l) | 547 (l) | 587(l) | 644 (l) |
| *m*TCPP | 419 (l) | 514 (l) | 548 (l) | 589 (l) | 645 (l) |
| | | 523 (s) | 560 (s) | 598 (s) | 657 (s) |
| 17*m*TCPP-CN | – | 527 (s) | 564 (s) | 600 (s) | 660 (s) |
| 9*m*TCPP-CN | – | 527 (s) | 565 (s) | 601 (s) | 661 (s) |
| 6*m*TCPP-CN | – | 526 (s) | 565 (s) | 600 (s) | 660 (s) |
| 5*m*TCPP-CN | – | 527 (s) | 563 (s) | 600 (s) | 660 (s) |

As shown in Fig. 2A and Table 1, the position of the absorption peaks of the porphyrins in DMF solution are not strongly affected by the presence or position of the carboxyl groups present at the periphery of the porphyrin. However, a small red shift in the Soret, $Q_I$ and $Q_{II}$ absorption bands is observed when passing from TPP to the *p*TCPP and *m*TCPP porphyrins (Table 1). On the other hand, the $Q_{III}$ and $Q_{IV}$ absorption bands of the *p*TCPP and *m*TCPP porphyrins are slightly shifted to the blue in comparison with TPP. Yet, the $Q_{III}$ and $Q_{IV}$ absorption bands of the *m*TCPP porphyrin show a small red shift regarding to the *p*TCPP. In what concerns the spectra of porphyrins in solid state (Fig. 2B), the intensity of the absorption bands follows the order TPP < *p*TCPP < *m*TCPP. The highest absorption intensities presented by *m*TCPP may be owing to the contribution of the *meso*-phenyl groups bearing *meta*-carboxy substituents at the porphyrin periphery [56]. Additionally, the Q absorption bands of the *p*TCPP and *m*TCPP (Table 1) in the solid state are red shifted when compared with those in solution. Yet, the peaks are well defined as it occurs in liquid phase, with exception of TPP bands that lack definition. The red shift of these bands may be explained by aggregation (J-aggregation), typical of these molecules [57].

The UV–vis diffuse reflectance spectra (DRS) of the semiconductor CN and of the porphyrin-CN hybrids loaded with 17 wt.% of the *free-base* porphyrins TPP, *m*TCPP and *p*TCPP are given in Fig. 2C. As

illustrated, CN exhibits absorption from UV through the visible region up to 450 nm, corresponding to a band gap of 2.7 eV, in accordance with literature [9]. After sensitization with TPP, *m*TCPP and *p*TCPP (Fig. 2C), the spectra of the hybrids 17TPP-CN, 17*p*TCPP-CN and 17*m*TCPP-CN show the combined features of the CN and porphyrin absorption. Besides, an increase in absorbance intensity in the whole region of the spectra is observed for the hybrids when comparing with pure CN. Furthermore, hybrid 17*m*TCPP-CN presents the highest absorbance intensity among the three, this relation being in accordance with the spectra of the pure porphyrins (Fig. 2B). In addition, 17*m*TCPP-CN and 17*p*TCPP-CN hybrids present four defined Q bands, as opposed to hybrid 17TPP-CN (Fig. 2C). Unlike hybrids 17*m*TCPP-CN and 17*p*TCPP-CN, that have charged carboxylic groups, the porphyrin of hybrid 17TPP-CN lacks these groups in its structure and it is more prone to aggregation [57]. It is known that the existence of peripheral carboxyphenyl groups difficults aggregation and facilitates the anchoring or adsorption of the porphyrins onto CN surface due to the formation of covalent or non-covalent interactions, respectively [42]. Having this in mind, and in order to evaluate the influence of these carboxyphenyl groups on the photocatalytic $H_2$ production, preliminary photocatalytic studies were conducted using the *as*-prepared hybrids of TPP-CN, *m*TCPP-CN and *p*TCPP-CN loaded with 17 wt.% of porphyrin. Specific surface area and pore properties are known to play an important role in photocatalytic reactions. We investigated these properties through $N_2$ adsorption-desorption measurements at 77 K. The $N_2$ adsorption-desorption isotherms and the BJH pore size distribution curves are given in Fig. S1 (Supplementary information), while the BET (Brunauer-Emmett–Teller) specific surface area ($S_{BET}$) and the pore volume results are compiled in Table S1 (Supplementary information). As displayed in Fig. S1, these isotherms are of Type II [58], resulting from the physisorption of the gas in a mostly macroporous adsorbent. All the curves present hysteresis loops of type H3, which is associated with slit-like mesopores formed as a result of aggregation of plate-like particles. The pore size distribution curves (inset Fig. S1) show a wide range of pore diameter from 3 to 70 nm, supporting the existence of mesopores and macropores [58,59]. As indicated in Table S1, the *as*-prepared CN presents a surface area of 11 $m^2\,g^{-1}$, similar to reported in literature [11]. When comparing to the bulk CN, the $S_{BET}$ of the hybrid 17TPP-CN decreased to 8 $m^2\,g^{-1}$, whereas an increase of the $S_{BET}$ was observed for the hybrids 17*m*TCPP-CN and 17*p*TCPP-CN (15 and 14 $m^2\,g^{-1}$, respectively). These results seem to suggest that the TPP porphyrin covers the surface of CN, forming aggregates (visible by the UV–vis DRS given in Fig. 2B), whereas the presence of the carboxyphenyl groups facilitates its adsorption on the mesopore structure of CN, increasing the surface area and providing more active site for $H_2$ production.

Based on the photocatalytic results (discussed ahead on the text), the best performing hybrid photocatalyst (*m*TCPP-CN) was subject to detailed studies in order to elucidate the mechanism of $H_2$ production. Since it is known that the amount of dye loaded on the semiconductor influences the production of $H_2$ [20], hybrid photocatalysts of *m*TCPP-CN were prepared with different wt.% of *m*TCPP (see experimental section for details). Accordingly, and henceforth, all the results and discussion concern the hybrid photocatalyst *m*TCPP-CN loaded with 17, 9, 6 and 5 wt.% of *m*TCPP. The UV–vis DRS of pure CN and *m*TCPP, and of the various X*m*TCPP-CN hybrids is illustrated in Fig. 2D and the peak position of the hybrids is presented in Table 1. As observed in Fig. 2D, the various X*m*TCPP-CN hybrids extend the absorption into the visible region when compared to CN, allowing a more efficient utilization of solar light to create photogenerated electrons and holes. Moreover, as the loading amount (wt.%) of *m*TCPP increases in the *m*TCPP-CN hybrid, the absorbance intensities of the hybrids is enhanced (Fig. 2D) and the Q bands of the *m*TCPP porphyrin in the hybrids are red shifted as compared to the pure porphyrin (Fig. 2D, Table 1). These observations are indicative of π-π stacking interactions between *m*TCPP and the semiconductor CN within the hybrid [42,44]. Thus, it can be inferred

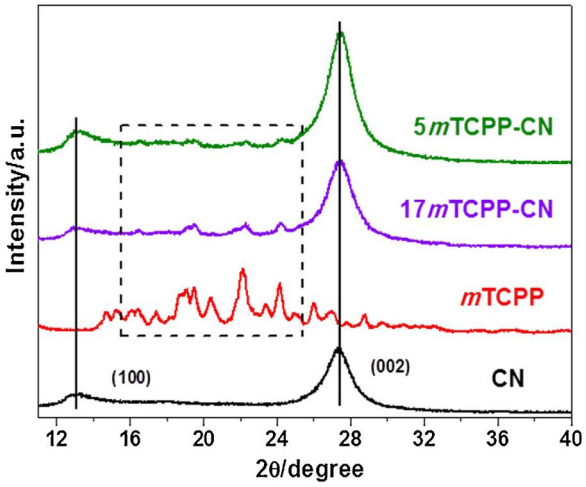


**Fig. 3.** XRD diffraction patterns of pure CN and *m*TCPP, and of 5*m*TCPP-CN and 17*m*TCPP-CN hybrids.

that *m*TCPP was successfully assembled onto the surface of the semiconductor.

The crystal structure of the materials CN, *m*TCPP and of *m*TCPP-CN hybrids loaded with 17 and 5 wt.% of porphyrin was studied by means of powder X-ray diffraction (XRD). As shown in Fig. 3, CN presents two distinct diffraction peaks located at 12.8° (diffraction plane 100) and 27.6° (diffraction plane 002) corresponding to the characteristic interplanar stacking peaks of aromatic systems and the interlayer structural packing, respectively [9,42]. The *m*TCPP porphyrin, on other hand, presents many diffraction peaks typical of this type of material. As for the 17*m*TCPP-CN and 5*m*TCPP-CN hybrids, these continue to present the characteristic peaks of CN (12.8° and 27.6°), in addition to a few new peaks at 16.4°, 19.4°, 22.2° and 24.2° (highlighted area in Fig. 3), representative of the porphyrin. Nevertheless, it is possible to note that although these peaks are present in both hybrids, they are more intense in the hybrid 17*m*TCPP-CN rather than in the hybrid 5*m*TCPP-CN, probably due to the higher content of porphyrin in the former composite. These results demonstrate that the sensitization does not influence the crystal structure of CN and reinforce the non-covalent nature of the interactions between the porphyrin and the semiconductor.

FTIR was used to study the molecular structure of *m*TCPP porphyrin adsorbed on the surface of CN in the hybrid 17*m*TCPP-CN (highest wt.% porphyrin load). For comparison purposes, the functional groups of pure CN and pure *m*TCPP were also characterized by ATR/FTIR, as depicted in Fig. 4. As illustrated, CN presents a sharp peak located at

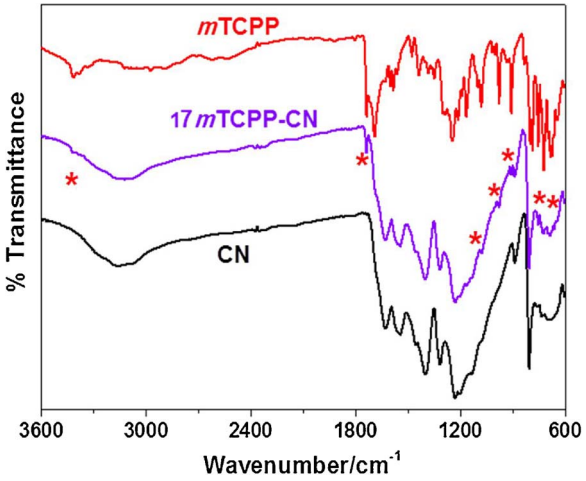


**Fig. 4.** FTIR spectra of pure CN and *m*TCPP, and of 17*m*TCPP-CN hybrid.

801 $cm^{-1}$, representative of triazine ring units [38,60] as well as a broad band ranging from 3000 to 3400 $cm^{-1}$ attributed to the stretching vibrations of hydroxyl groups of surface adsorbed water molecules, and to the N−H stretches due to the free amino groups [61]. The absorption band at 1640 $cm^{-1}$ is attributed to the C−N stretching vibration while four other bands located between 1200 and 1570 $cm^{-1}$ correspond to the typical stretching vibration modes of C−N heterocycles. The spectrum of the *m*TCPP porphyrin shows typical vibration bands in the range 600–1500 $cm^{-1}$ attributed to the symmetrical and asymmetric stretching of the pyrrole ring, namely $\nu$ (N−H), $\nu$ (C−H), $\nu$ (C═C) and $\nu$ (C═N) [60]. Additionally, the porphyrin also presents vibrational bands at 1734 and 1163 $cm^{-1}$ characteristic of the $\nu$ (C═O) and $\nu$ (C−O) stretch of carboxylic acid groups [60,62]. The peaks at 3300 and 3415 $cm^{-1}$ are assigned to the stretching vibration of the N−H bonds at the center of the porphyrin ring and to the OH stretching modes of the acid group, respectively [60]. After hybridization with the porphyrin *m*TCPP, all the vibrational bands of CN are still present, suggesting that this component did not suffer any structural change. Moreover, the spectra shows bands related with both materials (marked as * in Fig. 4), as is the case of the peak at 3415 $cm^{-1}$, indicating the successful formation of the *m*TCPP-CN hybrid by physical adsorption.

The surface morphology of CN, *m*TCPP and of the hybrid 17*m*TCPP-CN was investigated by SEM and TEM analysis (Fig. 5). As shown in Fig. 5A and B, CN presents typical porous sheet-like structure assembled as compact and irregular aggregates [59], resulting from the stacking of g-$C_3N_4$ layers, giving rise to a material with low $S_{BET}$. Different from CN, the porphyrin *m*TCPP (Fig. 5C and D) presents a flat open layered shape. The morphology of the 17*m*TCPP-CN hybrid (Fig. 5E and F) maintained the layered structure of CN, however, contrary to pure CN, the staking of graphitic-like $C_3N_4$ layers are well organized in plates. Even though the presence of the porphyrin is not evident in the image, probably due to the low ratio of porphyrin to CN, its presence has been proved by other techniques (UV-vis, XRD, TFIR, XPS, PL). Moreover, and due to the flat shape of the porphyrin, it is possible that this forms monolayers on CN surface, enhancing the overall photocatalyic efficiency due to the close contact of both components.

The chemical composition of the materials (CN and *m*TCPP) and the surface bonding interactions of each component within the hybrid 17*m*TCPP-CN were investigated by X-ray photoelectron spectroscopy (XPS). The survey and high-resolution XPS spectra (C1s, N1s, O1s) of the hybrid 17*m*TCPP-CN is depicted in Fig. 6 while the XPS spectra of CN and *m*TCPP is given in supplementary information (Fig. S2 and S3, respectively). The XPS survey spectra of the three materials (Figs. 6A, S2A, S3A) confirmed that all the samples are composed only by C, N and O elements, without any other impurities. The atomic ratios C:N calculated by XPS for CN, *m*TCPP and 17*m*TCPP-CN (Table S2) were of 0.71 (close to theoretical value of 0.75), 11.1 and 1.6, respectively. It is worthy to note that the C:N atomic ratio results in all the cases very close to the expected value, even for the hybrid, taking in account the ratio of 17*m*TCPP:CN used (15:75). The C1s XPS spectrum of pure CN (Fig. S2B) presents four peaks at binding energies of 294.1, 288.5, 286.3 and 284.9 eV [9,15,63]. The dominant peak at 288.5 eV (labeled C2 in Fig. S2B) corresponds to the tertiary carbon (−N−C═N-) in the lattice of CN [9]. The weak peak C1 centered at 294.1 eV corresponds to the π electron delocalization in $C_3N_4$ heterocycles, the C3 peak located at 286.3 eV is related to the $sp^3$-bonded defects on the g-$C_3N_4$ surface, as amino functional groups (C−$NH_2$) and the C4 peak at 284.9 eV is attributed to C(-N)$_3$ planar trigonal carbon geometry. The N1s XPS spectrum of CN (Fig. S2C) is deconvoluted into four peaks centered at 404.9 (N1), 401.5 (N2), 400.0 (N3) and 399.0 (N4) eV, in agreement with reported data [15]. The most abundant peak at 399.0 eV (N4) corresponds to the $sp^2$-bonded N in the triazine rings (C−N═C) while the second most abundant peak (N3) reveals the presence of tertiary nitrogen in N−(C)$_3$ units, reflecting the polymerization of dicyandiamide into CN [64]. The N1s core levels at 401.5 and 404.9 eV corresponds to C−$NH_x$ (amino functional groups) and to terminal nitrate groups, charging effects, or π excitations, respectively [61]. A residual O1s peak (Fig. S2D) at 532.4 eV can be attributed to adsorbed $H_2O$, $CO_2$ and $O_2$ to CN surface during the process of polymerization [15,61]. The C1s high-resolution XPS spectrum of the porphyrin *m*TCPP (Fig. S3B) shows four peaks with binding energies of 289.2 (C1), 288.1 (C2), 285.3 (C3) and 284.9 (C4) eV. The most abundant peak C4 corresponds to the $sp^2$ C−C bonds according to the literature [65]. Its N1s XPS spectrum (Fig. S3C) reveals two peaks at 400.1 (N1) and 398.1 (N2) eV, typical of *free-base* porphyrins, the imine nitrogen (−C═N-) of pyrrole and the pyrrolic nitrogen (-NH-), respectively. Both of these binding energies are similar to the ones reported in literature [65–68]. The O1s XPS spectrum (Fig. S3D) shows two peaks at 533.7 (O1) and 532.0 (O2) eV ascribed to the aromatic C−OH and (C−C═O) groups [65], respectively. Upon hybridization of CN with the porphyrin (Fig. 6), the C1s and N1s XPS spectra (Fig. 6B and C) of the hybrid presents the same four binding peaks as of the pure compounds, however, the peaks are shifted to higher binding energies by 0.4-0.5 eV. Similarly, the two peaks of the O1s ascribed to the porphyrin are also shifted to higher

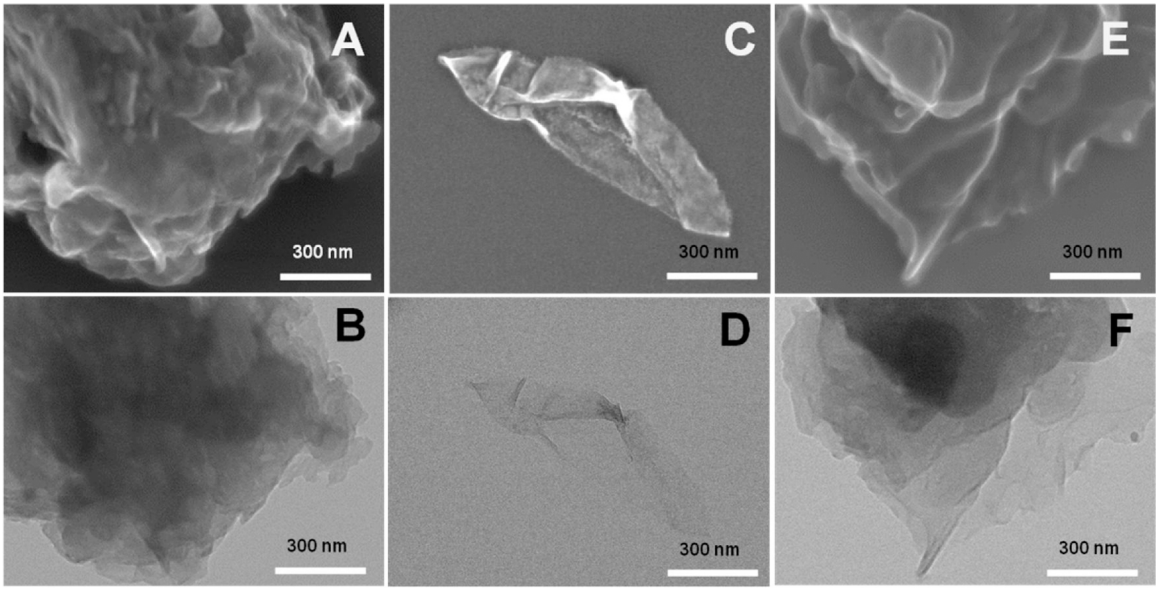


**Fig. 5.** SEM (A, C, E) and TEM images (B, D, F) of CN (A, B), *m*TCPP (C, D) and 17*m*TCPP-CN (E, F), respectively.

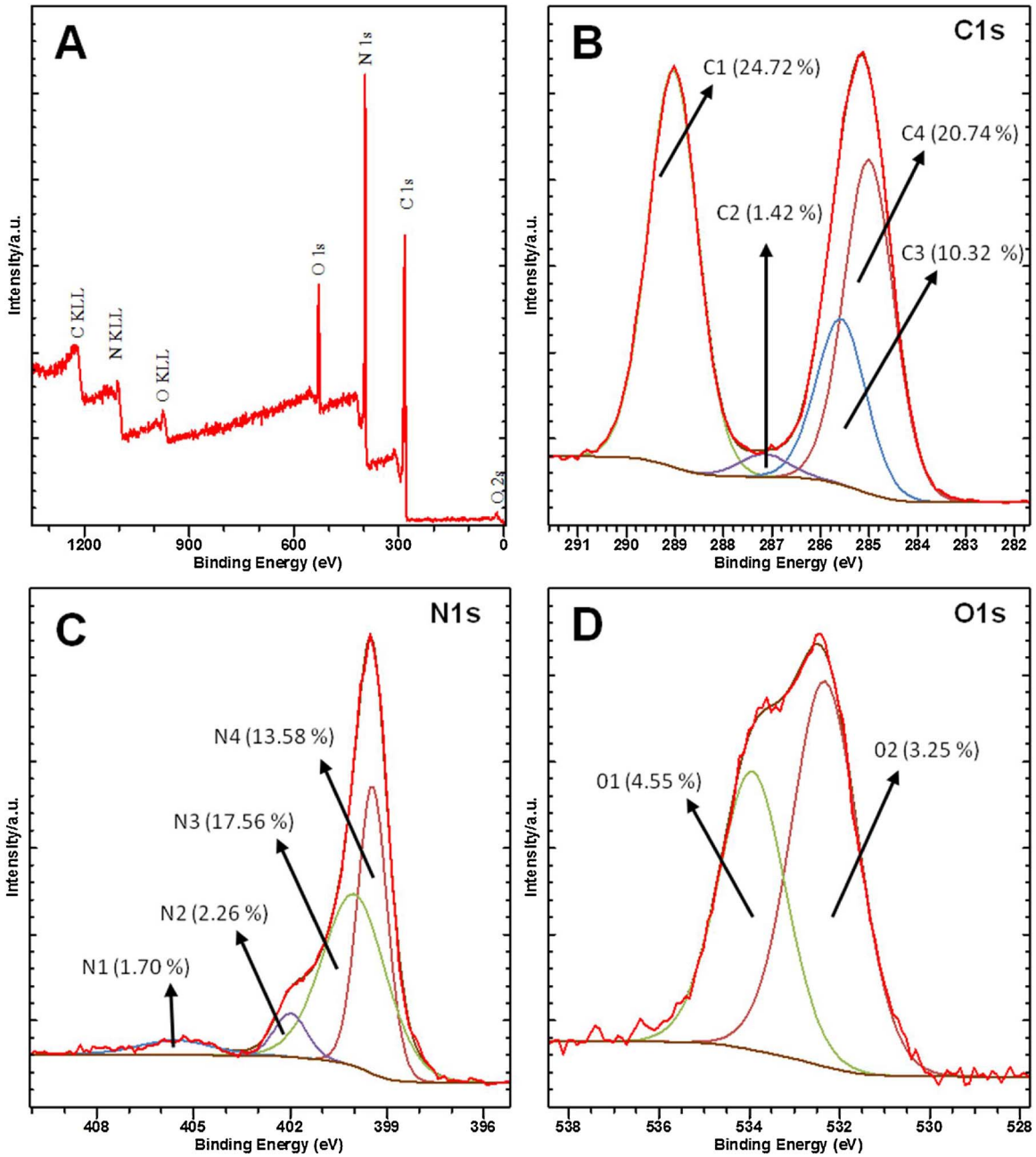


**Fig. 6.** XPS survey (A) and C1s (B), N1s (C) and O1s (D) high-resolution spectra of the hybrid 17*m*TCPP-CN (the relative abundance percentage is indicated for each element).

binding energies by 0.3 eV. Moreover, the relative intensity of these two peaks (Table S2) is roughly two times lower than the one obtained for pure porphyrin. This indicates the presence of the porphyrin on the surface of CN and suggests the existence of surface π-π interactions between CN and *m*TCPP.

Elemental analysis (EA) of CN, *m*TCPP and 17*m*TCPP-CN revealed a C:N molar ratio of 0.66, 12 and 0.97, respectively, as listed in Table S1. The C:N ratio of CN was relatively lower than the theoretical value of perfect carbon nitride (0.75). However, the H element (1.5 At%) was also detected for this material during EA measurement besides C and N elements. The existence of hydrogen element in the form of N—H and $NH_2$ groups which was confirmed by FTIR analysis can account for the lower C to N ratio. Additionally, C:N ratio for the porphyrin is close to the theoretical value while the ratio of the hybrid is also consistent with the ratio of porphyrin loaded on CN.

Photoluminescence (PL) [69,70] was used to investigate the excited state interactions between the *m*TCPP porphyrin and the semiconductor CN within the hybrid (Fig. 7).

The emission spectra of pure CN and *m*TCPP in water, and of the hybrid 17*m*TCPP-CN (as example), obtained upon excitation at 350 nm are displayed in Fig. 7A. CN presents a strong and wide emission band with maximum at 436 nm due to the band gap recombination of electron/hole pairs [38]. When the *m*TCPP porphyrin is excited at 350 nm, fluorescence emission is observed at higher wavelengths, in the region of 600–750 nm, with maximum centered at 640 and 720 nm, associated with vibronic transitions of the Q levels [71] and can be observed for excitation into both the Soret or the $Q_I$ absorption bands. Concerning the emission spectrum of the *m*TCPP-CN hybrid (Fig. 7A), this shows the features of both compounds. However, in comparison with pure CN, the maximum emission of CN is red-shifted by 24 nm, which once again point towards the existence of π-π interactions between *m*TCPP and CN, comparable to those observed in the sensitization of g-$C_3N_4$ with zinc

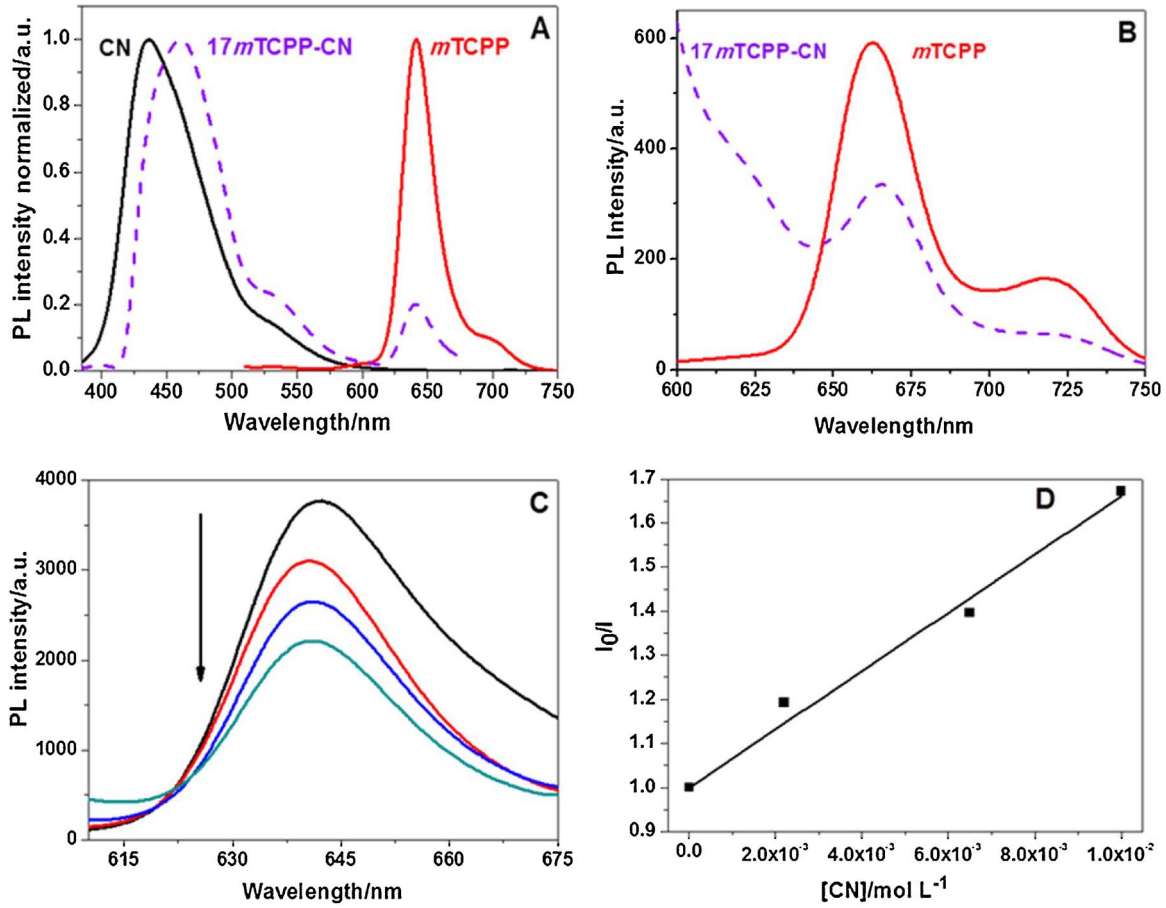


**Fig. 7.** (A) Normalized fluorescence emission spectra of the semiconductor CN, pure *m*TCPP and the 17*m*TCPP-CN hybrid in water (excitation at 350 nm) (B) Fluorescence emission spectra of pure *m*TCPP and of the 17*m*TCPP-CN hybrid in water (C) Steady-state fluorescence quenching of *m*TCPP aqueous solution ($1.0 \times 10^{-6}$ mol $L^{-1}$) in the presence of CN [$2.0 \times 10^{-3}$–$1.0 \times 10^{-2}$ mol $L^{-1}$] with excitation at 420 nm (D) Respective Stern-Volmer plot ($R^2 = 0.986$).

phthalocyanines [69]. The similar planar and π-conjugated structures of both *m*TCPP and CN, along with the presence of the carboxylic groups in the porphyrin that possess lone electron pairs, will increase the delocalization of electrons within the hybrid, leading to a change on the electronic states of the components, creating the red shift. As so, this shift of CN may be ascribed to the shift in the excited state potential compared to the ground state. It is important to note that this π-π interactions would lead to close interfacial connections between *m*TCPP-CN, which may serve as a more efficient electron migration path to promote the charge separation, and induce a synergetic effect to improve the photocatalytic activity.

Upon hybridization with CN (Fig. 7B), the fluorescence intensity of the *m*TCPP porphyrin within the 17*m*TCPP-CN hybrid decreases remarkably when compared with pure *m*TCPP. This fluorescence quenching indicates the occurrence of electron transfer between the excited state of the porphyrin, *m*TCPP*, and CN moieties in the hybrid, suggesting that the recombination rate of photogenerated charge carriers is lower. In order to corroborate this hypothesis, further quenching studies were carried out, in which different concentrations of CN were added to a *m*TCPP aqueous solution ($1.0 \times 10^{-6}$ mol $L^{-1}$) and the fluorescence intensity of *m*TCPP was monitored at its maximum wavelength of emission, 640 nm (Fig. 7C). As illustrated in Fig. 7C, the fluorescence intensity of the porphyrin decreases with the increase of CN concentration. The fluorescence quenching can be described by the well known Stern-Volmer relationship [72] (Eq. (3)):

$$\frac{I_0}{I} = 1 + K_{SV}[Q] = 1 + k_q\tau_0[Q] \quad (3)$$

where, $I_0$ and $I$ are the fluorescence intensities of the porphyrin in the absence and presence of quencher (CN), $\tau_0$ is the fluorescence lifetime of the porphyrin in the absence of the quencher CN, and $K_{SV}$ is the Stern-Volmer constant which is related to the bimolecular quenching rate constant ($k_q$) by the expression $K_{SV} = k_q\tau_0$. A good linear relationship was obtained for the Stern-Volmer plot in the range of CN concentration studied (Fig. 7D). Since $K_{SV}$ is given by the slope of the plot presented in Fig. 7D, and once the fluorescence lifetime of the porphyrin ($\tau_0$) was measured and equal to 9.59 ns (as discussed ahead in the text, Table 2), we can calculate the bimolecular quenching constant, $k_q$, using the Stern-Volmer equation. A value of $6.9 \times 10^9$ L $mol^{-1}$ $s^{-1}$ was obtained for $k_q$, indicative of efficient quenching of the porphyrin by the CN. Moreover, since the quenching rate approaches the rate of diffusion in water ($7.4 \times 10^9$ L $mol^{-1}$ $s^{-1}$ at 25° C [72]), we can infer that the quenching is due to a diffusive process. Furthermore, the absence of any overlap between the emission spectra of the *m*TCPP (640 nm) and the absorption spectrum of CN (320 nm, data not shown), in addition to the well-established electron accepting nature of CN (in the presence of excited electron donors namely the dyes), the hypothesis of electron transfer from the LUMO excited *m*TCPP to the conduction band of CN is well grounded. Thus, a higher separation efficiency of photogenerated electron-hole pairs will occur in the hybrid than in the pure CN.

The dynamic of electron recombination/transfer process between *m*TCPP and the semiconductor CN was further investigated using time-resolved fluorescence measurements. The emission decay kinetics of pure *m*TCPP and CN, and of the various *m*TCPP-CN hybrids were measured in aqueous solutions under excitation at 340 nm. The fluorescence decays of CN and of the porphyrin were monitored at 450 nm and 650 nm, respectively, while the fluorescence intensity decays of the

**Table 2**
Fluorescence intensity decay parameters of pure CN and *m*TCPP, and of the various *m*TCPP-CN hybrids as function of *m*TCPP loading (wt.%) ($\lambda_{ex}$ = 340 nm).

| $\lambda_{em}$ (nm) | Catalyst | $\alpha_1$ | $\tau_1$ (ns) | $\alpha_2$ | $\tau_2$ (ns) | $\alpha_3$ | $\tau_3$ (ns) | $\alpha_4$ | $\tau_4$ (ns) | $\tau_{av}$ (ns) | $\chi^2$ |
|---|---|---|---|---|---|---|---|---|---|---|---|
| 450 | CN | 0.39 | 0.24 | 0.37 | 0.97 | 0.22 | 3.0 | 0.04 | 11.4 | 4.77 | 1.11 |
| | 17*m*TCPP-CN | 0.28 | 0.26 | 0.38 | 0.93 | 0.28 | 2.9 | 0.06 | 10.3 | 4.94 | 1.30 |
| | 9*m*TCPP-CN | 0.30 | 0.26 | 0.38 | 0.99 | 0.28 | 3.1 | 0.05 | 11.8 | 5.31 | 1.03 |
| | 5*m*TCPP-CN | 0.27 | 0.23 | 0.39 | 1.0 | 0.28 | 2.9 | 0.06 | 10.8 | 5.20 | 1.07 |
| 650 | *m*TCPP | 1.00 | 9.6 | – | – | – | – | – | – | 9.59 | 1.09 |
| | 17*m*TCPP-CN | 0.28 | 0.06 | 0.07 | 2.4 | 0.66 | 9.7 | – | – | 9.52 | 1.16 |
| | 9*m*TCPP-CN | 0.52 | 0.01 | 0.11 | 1.3 | 0.37 | 9.7 | – | – | 9.35 | 1.10 |
| | 5*m*TCPP-CN | 0.22 | 0.07 | 0.09 | 1.7 | 0.69 | 9.7 | – | – | 9.48 | 1.23 |

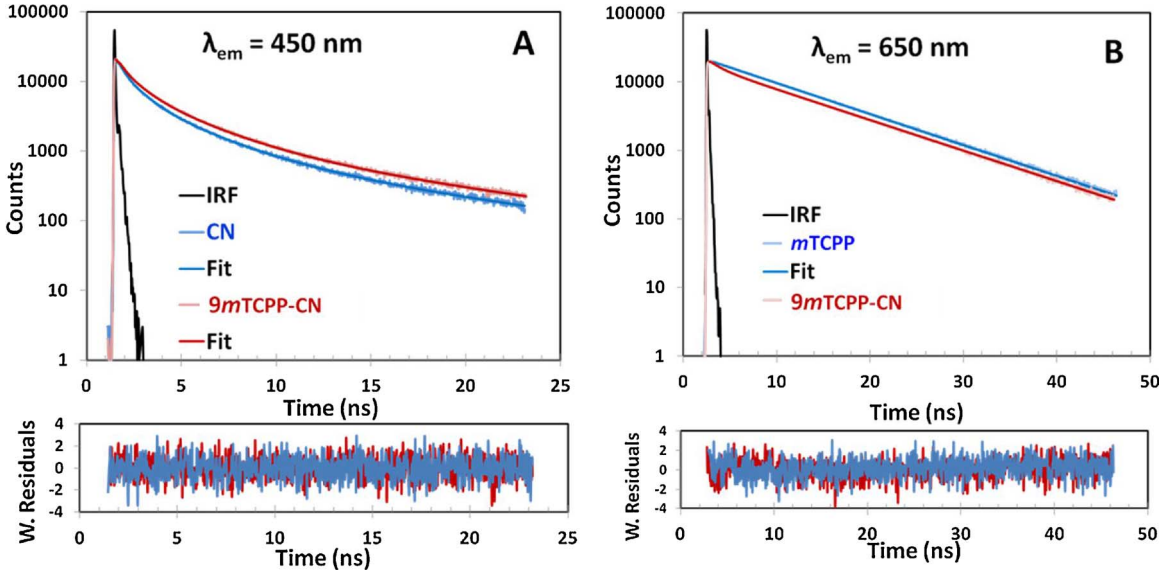


**Fig. 8.** Fluorescence intensity decays of (A) pure CN (blue) and the hybrid 9*m*TCPP-CN (red) ($\lambda_{em}$ = 450 nm) and (B) pure *m*TCPP (blue) and the hybrid 9*m*TCPP-CN (red) ($\lambda_{em}$ = 650 nm) in water. The IRF functions are depicted in black. The dark lines represent the best fit of a sum of exponentials to the experimental data. The weighted residuals of the fits are also shown. The excitation wavelength used in both cases was 340 nm.

various *m*TCPP-CN hybrids were collected at both wavelengths. The best fitting parameters to the experimental decays are gathered in Table 2. Fig. 8A and B show, as an example, the fluorescence intensity decays obtained at 450 nm and 650 nm for the aqueous solutions of pure CN and porphyrin and those measured for the hybrid 9*m*TCPP-CN samples, respectively.

According to the data listed in Table 2, the emission of pure *m*TCPP porphyrin at 650 nm decays mono-exponentially with an average lifetime of 9.59 ns, representative for this type of *free-base* porphyrin [57]. This mono-exponential decay indicates that the porphyrin exists in solution in its monomeric form and not as aggregates [57]. The emission decay of pure CN at 450 nm on the other hand, requires a four-exponential fit, presenting three components with short lifetimes (< 3.0 ns) and a very low component with a long lifetime (11.4 ns). The calculated average lifetime of 4.77 ns lies between the values reported in literature (3.75-5.66 ns) for the semiconductor CN [73]. Concerning the hybrids, its emission decay was studied at two different wavelengths, corresponding to the emission of CN (450 nm) and of the porphyrin (650 nm), in order to elucidate the influence of each component on the emission of the hybrid. In the three X*m*TCPP-CN hybrids indicated in Table 2, the emission of CN at 450 nm continues to follow a four-exponential decay and it is possible to note that the average lifetime ($\tau_{av}$) of CN increases with the decrease of the loading amount of *m*TCPP within the hybrid, reaching the highest fluorescence lifetime in the hybrid 9*m*TCPP-CN with a value of 5.31 ns. The emission of the porphyrin at 650 nm within the hybrids requires a tri-exponential fit rather than the mono-exponential fit obtained for the free porphyrin, suggesting that this additional contribution comes from CN. A careful analysis of data in Table 2 shows that the average fluorescence lifetime of the porphyrin within the hybrids decreases as the average fluorescence lifetime of CN increases, with the exception being the hybrid 9*m*TCPP-CN that present the highest emission lifetime for CN emitting at 450 nm (5.31 ns) and the lowest fluorescence lifetime for the porphyrin emitting at 650 nm (9.35 ns). This simultaneous decrease/increase of fluorescence lifetimes could be correlated with the injection of electrons from the porphyrin dye to conduction band of the semiconductor [70], decreasing in this way the recombination of the photogenerated $e^-/h^+$ and improving the interfacial charge transfer by increasing the fluorescence lifetime of CN, leading to the enhancement of the photocatalytic $H_2$ production activity. In fact, this interpretation of the kinetic data is consistent with the photocatalytic results that will be discussed in the next section, in which the hybrid 9*m*TCPP-CN exhibited the highest performance for the production of $H_2$.

### 3.2. Photocatalytic hydrogen generation

Dye sensitized photochemical $H_2$ production from water can be accomplished by using at least three molecular components such as a photosensitizer to act as light harvester and electron transfer component, an electron donor for dye regeneration and a $H_2$ evolving catalyst [20]. As so, the *as*-prepared hybrid photocatalysts were tested for $H_2$ production in aqueous media under UV–vis and visible light irradiation using EDTA as sacrificial electron donor and Pt as co-catalyst, at natural pH conditions (pH ~ 6.1). Primary photocatalytic experiments were performed with the hybrids 17TPP-CN, 17*m*TCPP-CN and 17*p*TCPP-CN under UV–vis light irradiation. The total amount of $H_2$ evolved under

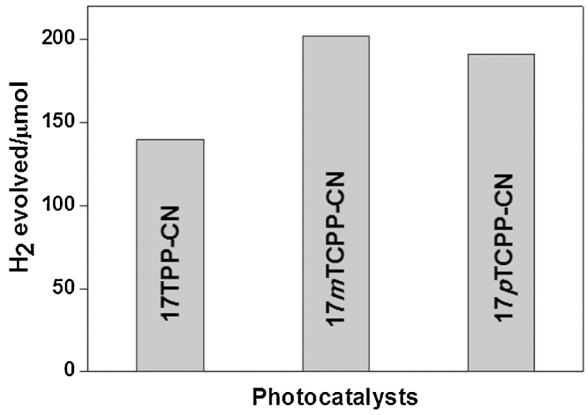


**Fig. 9.** Amount of $H_2$ photocatalytically generated over hybrids 17TPP-CN, 17*m*TCPP-CN and 17*p*TCPP-CN. Conditions: 15 mg of hybrid suspension containing EDTA ($2.0 \times 10^{-2}$ mol $L^{-1}$) and Pt ($6.1 \times 10^{-5}$ mol $L^{-1}$) at natural pH (pH ~ 6.1) after 6 h of UV–vis light irradiation.

these conditions after 6 h of photoreaction is presented in Fig. 9. These screening studies intended to evaluate the influence of porphyrin peripheral groups on the photocatalytic activity of the *as*-prepared materials, since it has been reported that the type and position of anchoring group attached to the semiconductor layer plays an important role in determining the performance of the dye [52].

Data presented in Fig. 9 reveal that substantial amounts of $H_2$ are evolved from any of these hybrid systems, following the order of 17*m*TCPP-CN (202 μmol) > 17*p*TCPP-CN (191 μmol) > 17TPP-CN (140 μmol). The highest amount of evolved $H_2$ was obtained with the hybrid containing the electron-withdrawing carboxyphenyl groups at the *meta*- position of the porphyrin periphery in detriment over the *para*- position. This result may be related to the aggregation of the *p*TCPP porphyrin dye in water, detected by UV–vis spectroscopy (not shown), which was not observed for the *m*TCPP porphyrin. Similar remarks were reported by Campbell *et al.* [74] which studied the effect of anchoring *meta*- and *para*-carboxyphenyl-substituted porphyrins at the surface of $TiO_2$ for application in DSSCs. The *meta*-substituted porphyrins did not show aggregation and lie flat on the $TiO_2$ conduction band, which significantly increases the efficiency when compared to those obtained using *para*-carboxyphenyl-substituted porphyrins. In the same way, Rochford *et al.*[75] also explored the effect of carboxyphenyl-substituent position (*meta*- and *para*-) of zinc porphyrins bonded to $TiO_2$ and to ZnO surface. It was concluded that *meta*-carboxyphenyl porphyrin derivatives do not undergo aggregation compared to *para*-carboxyphenyl porphyrin derivatives, leading to higher photocatalytic efficiency due to a greater charge injection into the semiconductor from porphyrin rings owing to its binding geometry that lie flat, and closer, to the semiconductor surface. Thus, the lowest amount of $H_2$ exhibited by the 17TPP-CN hybrid may be attributed to the facile aggregation of TPP porphyrin dye on the surface of CN (which can be noticed by the UV–vis DRS given in Fig. 2C) caused by the flat nature and large π system of TPP porphyrin, which usually results in rapid deactivation of the excited state [76]. Based on these above results obtained with the three hybrid systems, the hybrid presenting the best performance for photochemical $H_2$ production, *m*TCPP-CN, was selected to carry on further studies in order to clarify the mechanism of $H_2$ generation resulting from the dye sensitization. Another factor to take in account in dye sensitized $H_2$ production, in addition to the type/position of dye anchoring groups on the semiconductor surface discussed above, is the amount of porphyrin dye loaded on the semiconductor surface, as this plays an important role in trapping the CB electrons injected from porphyrin excited state, acting as active sites for promoting $H_2$ evolution and therefore suppressing the recombination of photogenerated carriers from the CB to the oxidized porphyrin [20,43]. Hence, *m*TCPP-CN hybrids containing different wt.% of *m*TCPP (17, 9, 6 and 5%) were tested for the photocatalytic hydrogen generation in the presence of EDTA and Pt, during 6 h of irradiation. Fig. 10A shows the evolution curves for the total amount of $H_2$ produced during 6 h while Fig. 10B compares the total amount of $H_2$ generated at the end of 6 h for the same hybrids.

As observed in Fig. 10A, all the curves present an initial induction time (15 min), probably due to *in situ* reduction of partially oxidized Pt nanoparticles by photogenerated hydrogen. After this period, a linear increase in $H_2$ production was observed corresponding to a steady state regime, after which an inflexion is observed for all the materials, around 120 min. This inflexion may be due to the faster depletion of EDTA, which is oxidized by the holes in both photoexcited porphyrin and CN. As shown in Fig. 10B, all the hybrids present markedly enhanced photoactivity compared to pure CN, indicative of efficient photosensitization of the dye porphyrins on the semiconductor CN. In this system, the porphyrin plays a dual role: as chromophore (to absorb light) and as charge carrier to inject directly electrons for CN. As the porphyrin load on the surface of CN increases so it does the absorption in visible region (see Fig. 2D), promoting electron transfer to CN, thus enhancing charge separation, as confirmed by fluorescence lifetime measurements (Table 2). The effects sum up increasing the generation of more conductive electrons and valence holes, synergistically contributing to increase the number of active sites available for $H_2$ production [43]. Moreover, although the hybrid loaded with 17 wt.% of

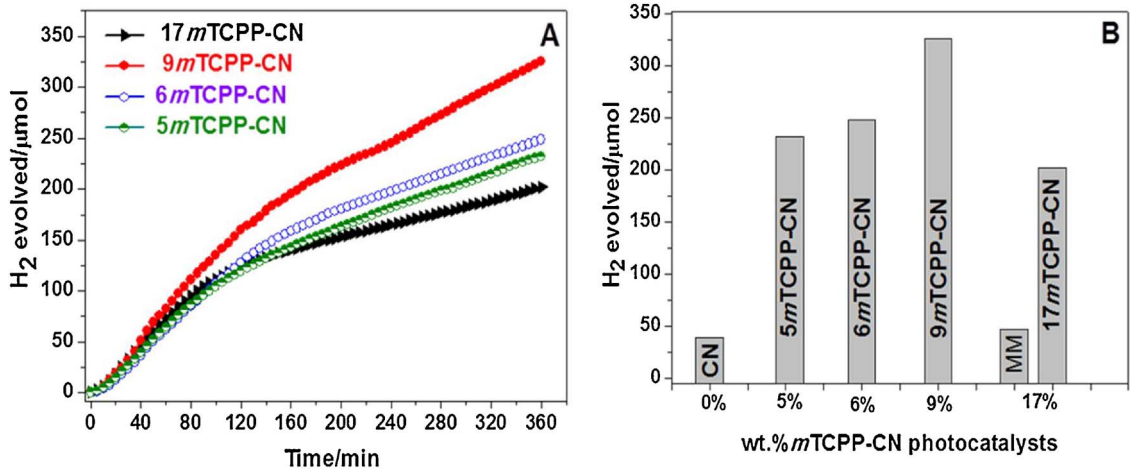


**Fig. 10.** (A) $H_2$ evolution profiles and (B) total amount of $H_2$ generated at the end of 6 h of irradiation for the various X*m*TCPP-CN hybrids. Conditions: 15 mg of hybrid suspension containing EDTA ($2.0 \times 10^{-2}$ mol $L^{-1}$) and Pt ($6.1 \times 10^{-5}$ mol $L^{-1}$) at pH ~ 6.1, under UV–vis light irradiation.

*m*TCPP has enhanced visible light absorption compared to that loaded with 9 wt.% of *m*TCPP, as expected from the application of the Beer-Lambert law, a decrease in the photocatalytic efficiency was observed. This decrease of the photocatalytic activity may be attributed to the agglomeration of the porphyrin surplus on the surface of the CN semiconductor, promoting back electron transfer within the porphyrin agglomerates, thus hindering the electron transfer from *m*TCPP to CN. This demonstrates that the amount of *m*TCPP has also a significant influence on the electron transfer process to CN, besides the influence on the light absorption properties. Additionally, the agglomerates may block the Pt sites, thus reducing the availability of surface active sites necessary for $H_2$ evolution [20]. The optimum porphyrin load, 9 wt.%, originated the highest amount of $H_2$ evolved at the end of 6 h of the UV–vis irradiation, *i. e.* 326 μmol.

Control experiments were performed for the pure CN and porphyrin in absence of EDTA and there was no detectable production of $H_2$. However, when similar experiments were conducted in the presence of EDTA, CN was able to produce 39 μmol of $H_2$ after 6 h of irradiation (Fig. 10B) while no detectable response was obtained with the porphyrin *m*TCPP since there was no electron relay present in the solution [34]. These results highlight the importance of using a sacrificial agent responsible for the regeneration of the photogenerated holes, and an electron relay (CN in this case). Moreover, a mechanical mixture (MM, Fig. 10B) of CN and 17*m*TCPP with the same amount of each phase present at the 17*m*TCPPCN hybrid was also irradiated during 6 h in presence of EDTA ($2.0\times10^{-2}$ mol $L^{-1}$) and Pt ($6.1\times10^{-5}$ mol $L^{-1}$), resulting in a production of $H_2$ of merely 46.5 μmol (contrasting with 202 μmol obtained with the hybrid material). It is therefore evident the creation of a synergy effect resulting from the immobilization of the porphyrin at the surface of CN, which may be attributed to an enhanced charge transfer between both components.

It is well-known that the photoreaction conditions for $H_2$ production must be optimized for every system [20,77]. This is the case of Pt, for instance, which is generally used as a co-catalyst and can significantly affect the activity for $H_2$ production. It is widely known that Pt-loaded sites on $TiO_2$ surfaces play an important role in trapping the CB electrons injected from the excited dyes, acting as active sites for $H_2$ production and suppressing the back electron transfer from the CB of $TiO_2$ to the oxidized dyes [78]. Consequently, the effect of Pt and pH on the photocatalytic activity of the hybrid 17*m*TCPP-CN was studied. When the hybrid was irradiated in the presence of EDTA at natural pH (pH 6.1), but increasing the concentration of Pt from $6.1\times10^{-5}$ mol $L^{-1}$ to $2.0\times10^{-4}$ mol $L^{-1}$, the amount of hydrogen evolved increased from 202 to 249 μmol after 6 h of irradiation (Fig. 11A), attributed to the increase in the amount of active sites for $H_2$ evolution. This increase is related with the ability of Pt to trap the conduction band electrons injected from porphyrin excited state, decreasing the recombination of the photogenerated electron/holes. Concerning the pH effect, and as expected, a decrease in the amount of $H_2$ evolved was observed as the medium become more alkaline, as depicted in Fig. 11B. Moreover, the maximum efficiency of $H_2$ production (221 μmol) was observed at pH 4.85. The reaction of hydrogen evolution involves the reduction of $H^+$ and donating ability of EDTA [79]. This pH-dependent hydrogen production is analogous to that reported in other studies [78].

Another important parameter in designing efficient catalysts for solar applications is their long term-stability. Therefore, the hybrid that showed best catalytic activity for $H_2$ production under UV–vis and visible light irradiation, 9*m*TCPP-CN, was subject to reuse studies. In each recycle, the reaction system is evacuated and irradiated for 6 h (Fig. 12A). After four consecutive recycles, the amount of hydrogen evolution over the hybrid is hardly changed, slightly decreasing its photocatalytic activity only in the last cycle (around 9.0%). This suggests that the hybrid photocatalyst presents good stability for a total of 24 h in the four consecutive runs with fresh solution periodically replaced in each run. This stability may be due to the efficient dye regeneration in the presence of EDTA as sacrificial reagent. Moreover, UV–vis absorption spectra of the hybrid suspension filtrate was measured after each photocatalytic experiment and no changes were observed, indicating that there is no dye present in the aqueous solution, supporting our previous assumptions that the porphyrin has been strongly adsorbed to the semiconductor.

The photocatalytic performance for $H_2$ evolution of the pure CN and of the hybrids 5*m*TCPP-CN and 9*m*TCPP-CN under visible light irradiation ($\lambda > 400$ nm) was tested. As shown in Fig. 12B, all the catalysts were able to produce $H_2$ using the same reaction conditions as previously used for UV–vis light irradiation. The total amount of $H_2$ evolved under 6 h of visible light irradiation is of nearly 6.0, 34 and 49 μmol for CN, 5*m*TCPP-CN and 9*m*TCPP-CN, respectively. The enhancement of $H_2$ production from the hybrids when compared to pristine CN can be attributed not only to the higher amount of photons absorbed by the porphyrin present in the hybrid since this extended the absorption into the visible region, but also by the fact that the electron transfer process between the porphyrin and the semiconductor was increased, diminishing therefore the recombination of electrons-holes pairs and increasing the catalytic activity. Moreover, the amount of porphyrin loaded on CN surface revealed again to be important for the photocatalytic activity, in which higher amount of $H_2$ was produced with the hybrid 9*m*TCPP-CN, in accordance with the previous results obtained under UV–vis irradiation.

Based on the results, a mechanism for the production of $H_2$ over the *m*TCPP-CN hybrid is proposed in Scheme 1. In aqueous solution, and under our experimental conditions, both porphyrin and CN can be excited and produce photogenerated $e^-$ and $h^+$. After absorption of light by the porphyrin, electrons are promoted from the ground state (HOMO

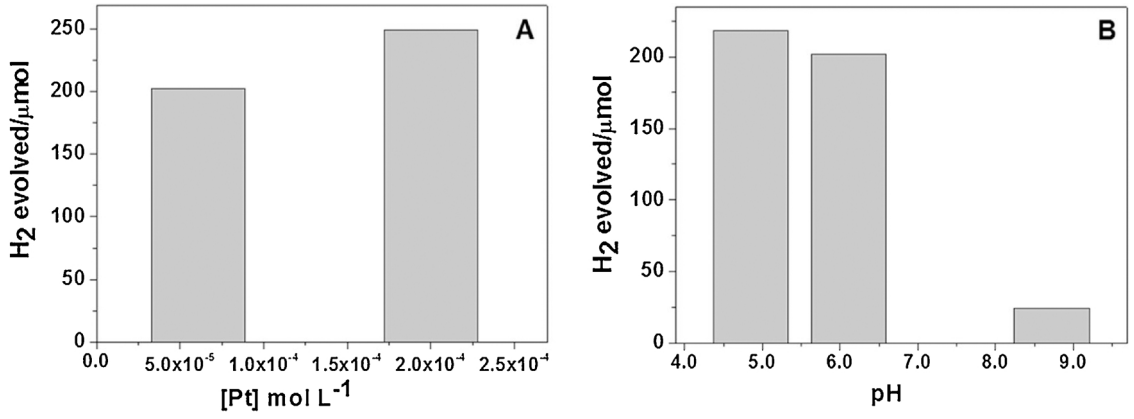


**Fig. 11.** Photocatalytic $H_2$ evolution for the hybrid 17*m*TCPP-CN as function of Pt concentration (A) and pH (B). Reaction conditions: 15 mg of catalyst, EDTA ($2.0\times10^{-2}$ mol $L^{-1}$) and (B) Pt ($6.1\times10^{-5}$ mol $L^{-1}$), 6 h of UV–Vis irradiation.

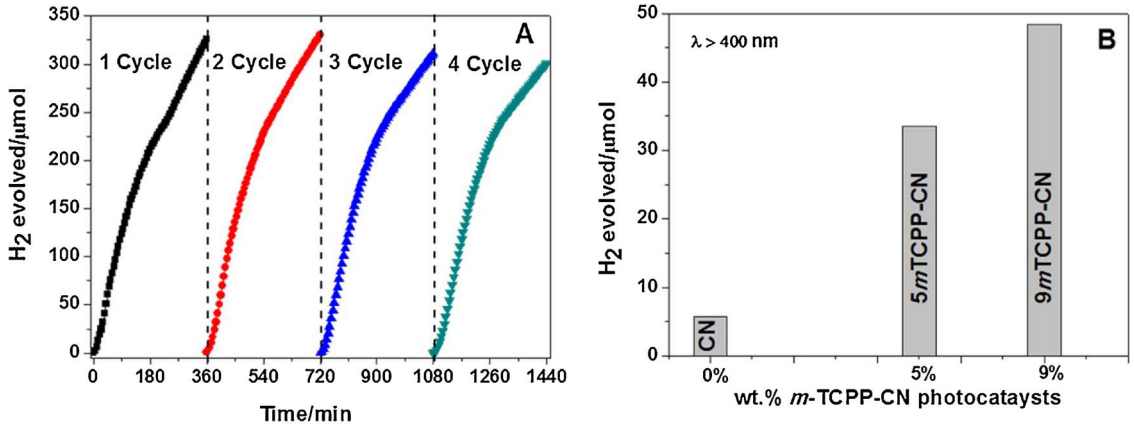


**Fig. 12.** (A) Cycle measurements of hydrogen evolution over the hybrid 9*m*TCPP-CN photocatalyst under UV–vis light irradiation. (B) Hydrogen production by pristine CN, and the hybrids 5*m*-TCPP and 9*m*TCPP-CN under 6 h of visible light ($\lambda > 400$ nm) irradiation. Reaction conditions: 15 mg of catalyst, EDTA ($2.0 \times 10^{-2}$ mol $L^{-1}$) and Pt ($6.1 \times 10^{-5}$ mol $L^{-1}$).

orbital) to the excited state (LUMO orbital). Once the porphyrin is in the excited state, *m*TCPP*, and according to the fluorescence results, electrons are transferred from the excited state of the porphyrin to the CB of the semiconductor CN and then to the Pt nanoparticles to carry out water reduction. The porphyrin excited state is quenched by the sacrificial electron donor EDTA back to the fundamental state. Pt nanoparticles act as CB electron sink reducing the $e^-/h^+$ pair recombination and promoting water reduction to form $H_2$ [10]. At the same time, CN can also be partially excited by absorbing photons with energy exceeding its band gap and subsequently transfer the electrons photogenerated in the CB directly to the Pt co-catalyst to generate $H_2$, while the $h^+$ photogenerated on the VB are scavenged by EDTA.

## 4. Conclusions

In this work, new nanohybrid photocatalysts of *free-base* porphyrins and bulk g-$C_3N_4$ were prepared by a non-covalent approach for production of hydrogen under UV–vis and visible light irradiation. Porphyrins (TPP, *m*TCPP and *p*TCPP) were easily hybridized with g-$C_3N_4$ through π–π stacking interactions while maintaining the electronic properties of the g-$C_3N_4$. The chemical structure of the porphyrins, with or without peripheral groups, as well as the amount of porphyrin loaded onto the surface of the semiconductor, along with the pH and amount of Pt, strongly influences the production of hydrogen. The mechanism of $H_2$ generation involves electron transfer from the excited state of the porphyrin to the conduction band of g-$C_3N_4$, facilitating therefore the separation and transport of the photogenerated charge carriers, thus enhancing the photocatalytic $H_2$ production activity.

This work demonstrates the promising application of graphitic carbon nitride sensitized with dye porphyrins for the visible photocatalytic hydrogen production from water. Furthermore, ongoing results suggest that the modification of CN structure and morphology are an effective way to both enhance the visible light harvesting capabilities and to further improve the transport and separation of photogenerated charge carriers, resulting in a more stable and photoactive hybrid catalyst.

## Acknowledgments

This work is a result of project “AIProcMat@N2020 – Advanced Industrial Processes and Materials for a Sustainable Northern Region of Portugal 2020”, with the reference NORTE-01-0145-FEDER-000006, supported by Norte Portugal Regional Operational Programme (NORTE

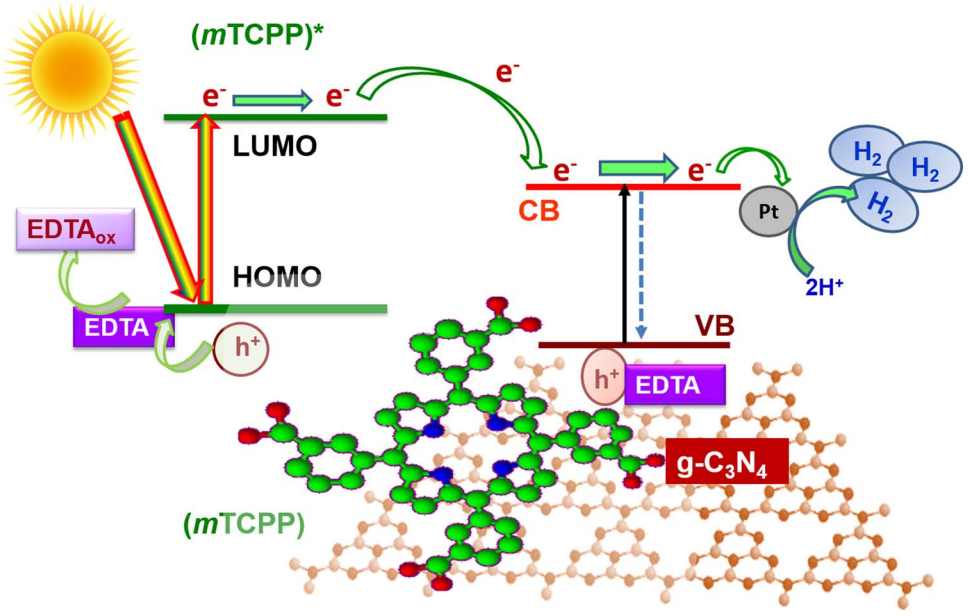


**Scheme 1.** Proposed mechanism for photocatalytic hydrogen production from water over CN sensitized with *m*TCPP porphyrin.

2020), under the Portugal 2020 Partnership Agreement, through the European Regional Development Fund (ERDF) and of Project POCI-01-0145-FEDER-006984–Associate Laboratory LSRE-LCM funded by ERDF through COMPETE2020 − Programa Operacional Competitividade e Internacionalização (POCI) − and by national funds through FCT − Fundação para a Ciência e a Tecnologia. M.P. and A.C. acknowledge FCT for project FAPESP/20107/2014. N.M.M.M and M.G.P.M.S.N. thank FCT/MEC for the financial support to the QOPNA research Unit (FCT UID/QUI/00062/2013), through national founds and when applicable co-financed by the FEDER, within the PT2020 Partnership Agreement and Compete 2020, and also to the Portuguese NMR Network. C.G.S. acknowledge the FCT Investigator Programme (IF/00514/2014) with financing from the European Social Fund and the Human Potential Operational Programme. N.M.M.M. thanks FCT for the Post-Doc scholarship SFRH/BPD/84216/2012. We are thankful to Dr. Carlos Sá and the CEMUP team (Portugal) for technical assistance and advice with XPS measurements.

## Appendix A. Supplementary data

Supplementary data associated with this article can be found, in the online version, at http://dx.doi.org/10.1016/j.apcatb.2017.08.079.

## References

[1] H. Zlotnik, D. Bloom, E. Jimenez, Seven Billion and Growing: The Role of Population Policy in Achieving Sustainability, United Nations, Department of Economic and Social Affairs, Population Division, New York, USA, 2011.
[2] P.D. Frischmann, K. Mahata, F. Wurthner, Chem. Soc. Rev. 42 (2013) 1847–1870.
[3] J. Barber, P.D. Tran, J. R. Soc Interface 10 (2013) 20120984, http://dx.doi.org/10.1098/rsif.2012.0984.
[4] A.A. Ismail, D.W. Bahnemann, Sol. Energy Mater. Sol. C 128 (2014) 85–101.
[5] J.J. Concepcion, R.L. House, J.M. Papanikolas, T.J. Meyer, Proc. Natl. Acad. Sci. U. S. A. 109 (2012) 15560–15564.
[6] S.I. Allakhverdiev, V. Thavasi, V.D. Kreslavski, S.K. Zharmukhamedov, V.V. Klimov, S. Ramakrishna, D.A. Los, M. Mimuro, H. Nishihara, R. Carpentier, J. Photochem. Photobiol. 11 (2010) 101–113.
[7] R.M. Navarro Yerga, M.C. Álvarez Galván, F. del Valle, J.A. Villoria de la Mano, J.L.G. Fierro, ChemSusChem 2 (2009) 471–485.
[8] S.J.A. Moniz, S.A. Shevlin, D.J. Martin, Z.-X. Guo, J. Tang, Energy Environ. Sci. 8 (2015) 731–759.
[9] X. Wang, K. Maeda, A. Thomas, K. Takanabe, G. Xin, J.M. Carlsson, K. Domen, M. Antonietti, Nat. Mater. 8 (2009) 76–80.
[10] S. Cao, J. Yu, J. Phys Chem. Lett. 5 (2014) 2101–2107.
[11] J. Wen, J. Xie, X. Chen, X. Li, Appl. Surf. Sci. 391 (2017) 72–123.
[12] W.-J. Ong, L.-L. Tan, Y.H. Ng, S.-T. Yong, S.-P. Chai, Chem. Rev. 116 (2016) 7159–7329.
[13] J. Zhang, X. Chen, K. Takanabe, K. Maeda, K. Domen, J.D. Epping, X. Fu, M. Antonietti, X. Wang, Angew. Chem. Int. Ed. 49 (2010) 441–444.
[14] S. Ye, R. Wang, M.-Z. Wu, Y.-P. Yuan, Appl. Surf. Sci. 358 (2015) 15–27.
[15] S. Cao, J. Low, J. Yu, M. Jaroniec, Adv. Mater. 27 (2015) 2150–2176.
[16] Y. Zhou, L. Zhang, J. Liu, X. Fan, B. Wang, M. Wang, W. Ren, J. Wang, M. Li, J. Shi, J. Chem. Mater. A 3 (2015) 3862–3867.
[17] Y. Bing, L. Qiuye, I. Hideo, K. Tetsuya, Y. Jinhua, Sci. Technol. Adv. Mater. 12 (2011) 034401.
[18] Y. Gong, J. Wang, Z. Wei, P. Zhang, H. Li, Y. Wang, ChemSusChem 7 (2014) 2303–2309.
[19] Q. Xiang, J. Yu, M. Jaroniec, J. Phys. Chem. C 115 (2011) 7355–7363.
[20] J. Willkomm, K.L. Orchard, A. Reynal, E. Pastor, J.R. Durrant, E. Reisner, Chem. Soc. Rev. 45 (2016) 9–23.
[21] P.V. Kamat, Chem. Rev. 93 (1993) 267–300.
[22] H. Hagiwara, T. Inoue, S. Ida, T. Ishihara, Phys. Chem. Chem. Phys. 13 (2011) 18031–18037.
[23] M.K. Panda, K. Ladomenou, A.G. Coutsolelos, Coord. Chem. Rev. 256 (2012) 2601–2627.
[24] E.D. Sternberg, D. Dolphin, C. Brückner, Tetrahedron 54 (1998) 4151–4202.
[25] H. Abrahamse, M.R. Hamblin, J. Biochem. 473 (2016) 347–364.
[26] E. Alves, M.A.F. Faustino, M.G.P.M.S. Neves, A. Cunha, J. Tome, A. Almeida, Med. Future Chem. 6 (2014) 141–164.
[27] M. Jurow, A.E. Schuckman, J.D. Batteas, C.M. Drain, Coord. Chem. Rev. 254 (2010) 2297–2310.
[28] L. Lvova, C. Di Natale, R. Paolesse, Sens. Actuators B 179 (2013) 21–31.
[29] N.M.M. Moura, C. Núñez, S.M. Santos, M.A.F. Faustino, J.A.S. Cavaleiro, M.G.P.M.S. Neves, J.L. Capelo, C. Lodeiro, Inorg. Chem. 53 (2014) 6149–6158.
[30] Y. Ding, Y. Tang, W. Zhu, Y. Xie, Chem. Soc. Rev. 44 (2015) 1101–1112.
[31] E. Silva, M.M. Pereira, H.D. Burrows, M.E. Azenha, M. Sarakha, M. Bolte, Photochem. Photobiol. Sci. 3 (2004) 200–204.
[32] G. Zhao, H. Pang, G. Liu, P. Li, H. Liu, H. Zhang, L. Shi, J. Ye, Appl. Catal. B 200 (2017) 141–149.
[33] L. Zhang, Y. Lu, Y. Du, P. Yang, X. Wang, J. Porphyr. Phthalocyanines 14 (2010) 540–546.
[34] K. Ladomenou, M. Natali, E. Iengo, G. Charalampidis, F. Scandola, A.G. Coutsolelos, Coord. Chem. Rev. 304–305 (2015) 38–54.
[35] L.R. Milgrom, The Colours of Life: An Introduction to the Chemistry of Porphyrins and Related Compounds, 1st ed., Oxford University Press, Oxford, 1997.
[36] W. Wang, J. Chen, C. Li, W. Tian, Nat. Commun. 5 (2014) 4647, http://dx.doi.org/10.1038/ncomms5647.
[37] S. Fukuzumi, T. Honda, T. Kojima, Coord. Chem. Rev. 256 (2012) 2488–2502.
[38] Y. Wang, J. Hong, W. Zhang, R. Xu, Catal. Sci. Technol. 3 (2013) 1703–1711.
[39] S. Min, G. Lu, J. Phys. Chem. C 116 (2012) 19644–19652.
[40] X. Zhang, L. Yu, C. Zhuang, T. Peng, R. Li, X. Li, ACS Catal. 4 (2014) 162–170.
[41] X. Zhang, T. Peng, L. Yu, R. Li, Q. Li, Z. Li, ACS Catal. 5 (2015) 504–510.
[42] D. Chen, K. Wang, W. Hong, R. Zong, W. Yao, Y. Zhu, Appl. Catal. B 166–167 (2015) 366–373.
[43] D.H. Wang, J.N. Pan, H.H. Li, J.J. Liu, Y.B. Wang, L.T. Kang, J.N. Yao, J. Chem. Mater. A 4 (2016) 290–296.
[44] M. Zhu, Z. Li, B. Xiao, Y. Lu, Y. Du, P. Yang, X. Wang, ACS Appl. Mater. Interfaces 5 (2013) 1732–1740.
[45] W.L.F. Armarego, D.D. Perrin, Purification of Laboratory Chemicals, 4th ed., Butterworth-Heinemann, Oxford, 1996.
[46] A.D. Adler, F.R. Longo, W. Shergalis, J. Am. Chem. Soc. 86 (1964) 3145–3149.
[47] A.D. Adler, F.R. Longo, J.D. Finarelli, J. Goldmacher, J. Assour, L. Korsakoff, J. Org. Chem. 32 (1967) 476.
[48] A.M.d.A.R. Gonsalves, J.M.T.B. Varejão, M.M. Pereira, J. Heterocycl. Chem. 28 (1991) 635–640.
[49] K.S. Akerfeldt, R.M. Kim, D. Camac, J.T. Groves, J.D. Lear, W.F. DeGrado, J. Am. Chem. Soc. 114 (1992) 9656–9657.
[50] N.M.M. Moura, C. Cuerva, J.A.S. Cavaleiro, R.F. Mendes, F.A. Almeida Paz, M. Cano, M.G.P.M.S. Neves, C. Lodeiro, ChemPlusChem 81 (2016) 262–273.
[51] C. Gomes Silva, I. Luz, F.X. Llabrés i Xamena, A. Corma, H. García, Chem. Eur. J. 16 (2010) 11133–11138.
[52] R.B. Ambre, S.B. Mane, G.-F. Chang, C.-H. Hung, ACS Appl. Mater. Interfaces 7 (2015) 1879–1891.
[53] F. D'Souza, O. Ito, Coord. Chem. Rev. 249 (2005) 1410–1422.
[54] G. Bottari, O. Trukhina, M. Ince, T. Torres, Coord. Chem. Rev. 256 (2012) 2453–2477.
[55] J.L. Humphrey, D. Kuciauskas, J. Am. Chem. Soc. 128 (2006) 3902–3903.
[56] M. Asha Jhonsi, A. Kathiravan, R. Renganathan, J. Lumin. 129 (2009) 854–860.
[57] R.F. Khairutdinov, N. Serpone, J. Phys. Chem. B 103 (1999) 761–769.
[58] M. Thommes, K. Kaneko, V. Neimark Alexander, P. Olivier James, F. Rodriguez-Reinoso, J. Rouquerol, S.W. Sing Kenneth, Pure Appl. Chem. 87 (2015) 1051–1069.
[59] M.S. Akple, J. Low, S. Wageh, A.A. Al-Ghamdi, J. Yu, J. Zhang, Appl. Surf. Sci. 358 (2015) 196–203.
[60] Y. Yuan, H. Lu, Z. Ji, J. Zhong, M. Ding, D. Chen, Y. Li, W. Tu, D. Cao, Z. Yu, Z. Zou, J. Chem. Eng. 275 (2015) 8–16.
[61] D.J. Martin, K. Qiu, S.A. Shevlin, A.D. Handoko, X. Chen, Z. Guo, J. Tang, Angew. Chem. 126 (2014) 9394–9399.
[62] Y.-J. Yuan, J.-R. Tu, Z.-J. Ye, H.-W. Lu, Z.-G. Ji, B. Hu, Y.-H. Li, D.-P. Cao, Z.-T. Yu, Z.-G. Zou, Dyes Pigm. 123 (2015) 285–292.
[63] B. Zhu, P. Xia, W. Ho, J. Yu, Appl. Surf. Sci. 344 (2015) 188–195.
[64] Q. Xu, B. Cheng, J. Yu, G. Liu, Carbon 118 (2017) 241–249.
[65] D.H. Karweik, N. Winograd, Inorg. Chem. 15 (1976) 2336–2342.
[66] D.K. Lavallee, J. Brace, N. Winograd, Inorg. Chem. 18 (1979) 1776–1780.
[67] J.R. Eskelsen, Y. Wang, Y. Qui, M. Ray, M. Handlin, K.W. Hipps, U. Mazur, J. Porphyr. Phthalocyanines 16 (2012) 1233–1243.
[68] H. Yamashige, S. Matsuo, T. Kurisaki, R.C.C. Perera, H. Wakita, Anal. Sci. 21 (2005) 635–639.
[69] L. Yu, X. Zhang, C. Zhuang, L. Lin, R. Li, T. Peng, Phys. Chem. Chem. Phys. 16 (2014) 4106–4114.
[70] M. Zhu, Y. Du, P. Yang, X. Wang, Catal. Sci. Technol. 3 (2013) 2295–2302.
[71] A.-M. Manke, K. Geisel, A. Fetzer, P. Kurz, Phys. Chem. Chem. Phys. 16 (2014) 12029–12042.
[72] M. Montalti, A. Credi, L. Prodi, M.T. Gandolfi, Hanbook of Photochemistry, third ed., CRC Press, Boca Raton, FL, 2006.
[73] H. Zhang, A. Yu, J. Phys. Chem. 118 (2014) 11628–11635.
[74] W.M. Campbell, A.K. Burrell, D.L. Officer, K.W. Jolley, Coord. Chem. Rev. 248 (2004) 1363–1379.
[75] J. Rochford, D. Chu, A. Hagfeldt, E. Galoppini, J. Am. Chem. Soc. 129 (2007) 4655–4665.
[76] L. Martin-Gomis, F. Fernandez-Lazaro, A. Sastre-Santos, J. Chem. Mater. A 2 (2014) 15672–15682.
[77] X. Chen, S. Shen, L. Guo, S.S. Mao, Chem. Rev. 110 (2010) 6503–6570.
[78] S.K. Choi, H.S. Yang, J.H. Kim, H. Park, Appl. Catal. B 121–122 (2012) 206–213.
[79] S. Stankovic, B. Grgur, N. Krstajic, M. Vojnovic, J. Electroanal. Chem. 549 (2003) 37–47.